AD-A145 834 FINITE-DIFFERENCE SYNTHETIC SEISMOGRAMS FOR SH WAVES (U) CALIFORNIA INST OF TECH PASADENA J VIDALE ET AL. 13 AUG 84 SCIENTIFIC-1 AFGL-TR-84-0082 F19628-83-K-0010 1/1

UNCLASSIFIED F/G 8/11 NL

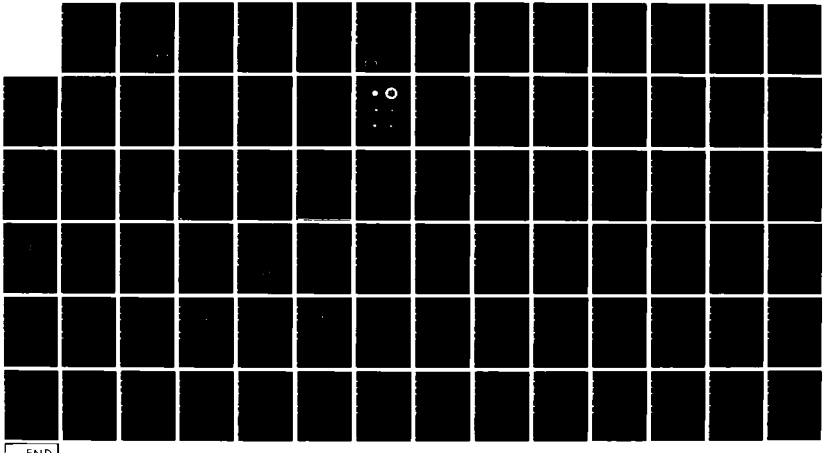

END

FILMED

DTIC

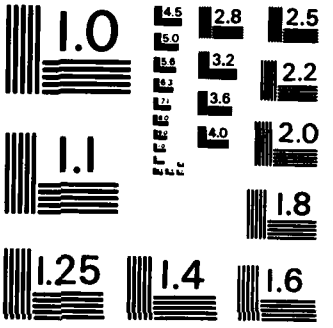


MICROCOPY RESOLUTION TEST CHART
NATIONAL BUREAU OF STANDARDS-1963-A

AD-A145 834

12

AFGL-TR-84-0082

# FINITE-DIFFERENCE SYNTHETIC SEISMOGRAMS FOR SH WAVES

J. Vidale
Don Helmberger
Rob Clayton

California Institute of Technology
1201 E. California Blvd
Pasadena, California 91125

Scientific Report No. 1

13 August 1984

Approved for public release; distribution unlimited

DTIC FILE COPY

DTIC ELECTE SEP 2 1 1984 S D

B

AIR FORCE GEOPHYSICS LABORATORY
AIR FORCE SYSTEMS COMMAND
UNITED STATES AIR FORCE
HANSCOM AFB, MASSACHUSETTS 01731

9 09 20 023

This report has been reviewed by the ESD Public Affairs Office (PA) and is releasable to the National Technical Information Service (NTIS).

This technical report has been reviewed and is approved for publication.

JOHN J. CIPAR
Contract Manager

HENRY A. OSSING, Chief
Solid Earth Geophysics Branch

FOR THE COMMANDER

DONALD H. ECKHARDT, Director
Earth Sciences Division

Qualified requestors may obtain additional copies from the Defense Technical Information Center. All others should apply to the National Technical Information Service.

If your address has changed, or if you wish to be removed from the mailing list, or if the addressee is no longer employed by your organization, please notify AFGL/DAA, Hanscom AFB, MA 01731. This will assist us in maintaining a current mailing list.

Do not return copies of this report unless contractual obligations or notices on a specific document requires that it be returned.

## REPORT DOCUMENTATION PAGE

| | |
|---|---|
| 1a. REPORT SECURITY CLASSIFICATION: Unclassified | 1b. RESTRICTIVE MARKINGS |
| 2a. SECURITY CLASSIFICATION AUTHORITY | 3. DISTRIBUTION/AVAILABILITY OF REPORT: Approved for public release; distribution unlimited |
| 2b. DECLASSIFICATION/DOWNGRADING SCHEDULE | |
| 4. PERFORMING ORGANIZATION REPORT NUMBER(S) | 5. MONITORING ORGANIZATION REPORT NUMBER(S): AFGL-TR-84-0082 |
| 6a. NAME OF PERFORMING ORGANIZATION: California Institute of Tech; 6b. OFFICE SYMBOL (If applicable) | 7a. NAME OF MONITORING ORGANIZATION: Air Force Geophysical Laboratory |
| 6c. ADDRESS (City, State and ZIP Code): 1201 E. California Blvd. Pasadena, CA 91125 | 7b. ADDRESS (City, State and ZIP Code): Hanscom AFB, Massachusetts 01731 Monitor/John J. Cipar/LWH |
| 8a. NAME OF FUNDING/SPONSORING ORGANIZATION; 8b. OFFICE SYMBOL (If applicable) | 9. PROCUREMENT INSTRUMENT IDENTIFICATION NUMBER: F19628-83-K-0010 |
| 8c. ADDRESS (City, State and ZIP Code) | 10. SOURCE OF FUNDING NOS. |

| PROGRAM ELEMENT NO. | PROJECT NO. | TASK NO. | WORK UNIT NO. |
|---|---|---|---|
| 62101F | 7600 | 09 | AE |

11. TITLE (Include Security Classification): Finite-Difference Synthetic Seismograms for SH Waves

12. PERSONAL AUTHOR(S): Vidale, J.; Helmberger, Don; Clayton, Rob

| 13a. TYPE OF REPORT | 13b. TIME COVERED | 14. DATE OF REPORT (Yr., Mo., Day) | 15. PAGE COUNT |
|---|---|---|---|
| Sci Rpt No. 1 | FROM _____ TO _____ | 1984 August 13 | 80 |

16. SUPPLEMENTARY NOTATION

| 17. COSATI CODES | | | 18. SUBJECT TERMS (Continue on reverse if necessary and identify by block number) |
|---|---|---|---|
| FIELD | GROUP | SUB. GR. | seismic waves, earthquake sources finite difference, numerical modeling |
| | | | |
| | | | |

19. ABSTRACT (Continue on reverse if necessary and identify by block number)

The research performed under this contract, during the period 12 January 1983 through 11 January 1984, can be divided into two major topics: Finite-Difference synthetic seismograms for SH waves; and array analysis of the ground motions from the 1971 San Fernando Earthquake.

In Section II, the accuracy and ease of application of the finite-difference method for generating synthetic siesmograms of SH wave propagation in cylindrically symmetric media is discussed. The finite-difference method has the advantage that arbitrary density and velocity field in the medium may be specified. A point source is generated by a simple transformation of a line source. The accuracy of the finite-difference seismograms in flat layered media is confirmed by comparison with the Cagniard De-Hoop method. The finite-difference seismograms also agree with a previously untried dipping-layer Cagniard method. An earthquake radiation pattern is approximated by introducing a "near-field" which has permanent displacement near the source.

| 20. DISTRIBUTION/AVAILABILITY OF ABSTRACT | 21. ABSTRACT SECURITY CLASSIFICATION |
|---|---|
| UNCLASSIFIED/UNLIMITED ☒ SAME AS RPT. ☐ DTIC USERS ☐ | Unclassified |

| 22a. NAME OF RESPONSIBLE INDIVIDUAL | 22b. TELEPHONE NUMBER (Include Area Code) | 22c. OFFICE SYMBOL |
|---|---|---|
| John Cipar, GS-13, Geophysicist | (617) 861-3746 | AFGL/LWH |

DD FORM 1473, 83 APR EDITION OF 1 JAN 73 IS OBSOLETE.

In Section III, the important new field of strong ground motion modeling is discussed, where velocity profiles recorded from the 1971 San Fernando earthquake demonstrate strong path effects due to topography of the basement surfaces. The different waveform pattern observed along three long profiles implies that valley or basin structures can produce significant reverberation and amplification effects. It is suggested that the proper geometry of basins and earthquake sources needs to be considered in order to predict waveforms along these wave paths.

SCIENTIFIC REPORT NO. 1.

January 12, 1983 - January 11, 1984

| | |
|---|---|
| Name of Contractor: | California Institute of Technology |
| Effective Date of Contract: | 11 January 1983 |
| Contract Expiration Date: | 11 January 1986 |
| Amount of Contract: | $273,547 |
| Contract Number: | F19628-83-K-0010 |
| Principal Investigators: | Donald V. Helmberger<br>(818) 356-6998 |
| | David G. Harkrider<br>(818) 356-6910 |
| | Robert W. Clayton<br>(818) 356-6909 |
| Program Manager and Telephone Number: | Dr. John Cipar<br>(617) 861-3748 |
| Short Title of Work: | Interaction of Seismic Waves With Complex Structures |

The views and conclusions contained in this document are those of the authors and should not be interpreted as necessarily representing the official policies.

Sponsored by
Solid Earth Geophysics Branch
Earth Sciences Division
Department of the Air Force
Air Force Geophysics Laboratory (AFSC)
Hanscom Air Force Base, Massachusetts 01731

DTIC
ELECTE
SEP 2 1 1984
S D

Accession For
NTIS GRA&I ☑
DTIC TAB ☐
Unannounced ☐
Justification
By
Distribution/
Availability Codes
Dist | Avail and/or Special
A-1

Table of Contents


| | | Page |
|---|---|---|
| I. | Summary | 1 |
| II. | Finite-Difference Synthetic Seismograms for SH Waves | 3 |
| III. | Array Analysis of the Ground Motions from the 1971 San Fernando, California Earthquake | 33 |

## I. Summary

The research performed under this contract, during the period 12 January 1983 through 11 January 1984, can be divided into two major topics; Finite-Difference synthetic seismograms for SH waves; and array analysis of the ground motions from the 1971 San Fernando Earthquake.

In section II, the accuracy and ease of application of the finite-difference method for generating synthetic seismograms of SH wave propagation in cylindrically symmetric media is discussed. The finite-difference method has the advantage that arbitrary density and velocity fields in the medium may be specified. A point source is generated by a simple transformation of a line source. The accuracy of the finite-difference seismograms in flat layered media is confirmed by comparison with the Cagniard De-Hoop method. The finite difference seismograms also agree with a previously untried dipping-layer Cagniard method. An earthquake radiation pattern is approximated by introducing a "near field" which has permanent displacement near the source.

In section III, the important new field of strong ground motion modeling is discussed, where velocity profiles recorded from the 1971 San Fernando earthquake demonstrate strong path effects due to topography of the basement surfaces. The different waveform pattern observed along three long profiles implies that valley or basin structures can produce significant reverberation and amplification effects. It is suggested that the proper geometry of basins and earthquake sources needs to be considered in order to predict waveforms along these wave paths.

Velocity profiles along three local arrays in the Los Angeles basin suggests that, within 3 km in range, the waveforms are almost identical. It is also suggested that higher frequency waves, as represented by ground accelerations, are less affected by these large scale basin structures.

Profiles of displacement traces, which are not shown in this study, display characteristics similar to those observed in the velocity profiles. That is, the waveforms show good correlation with variations in the basement surfaces. However, due to its high-frequency nature, the S phase is more easily recognized in velocity records than in displacement records.

We use the 2D finite difference method to compute synthetic seismograms for irregular structures which exist along the various profiles. Although the structure used in the calculation is rather simplified and the numerical code is for acoustical media, the general features of the synthetics agree quite well with the observed ground motions. We approximate Heaton's (1982) source model, which has two major areas of dislocation by point sources, at depths of 13 km and 1 km. Using the relative timing, amplitude and signal duration of major arrivals observed in the ground motions along both profile I and profile II, we suggest that the coherent S phase (the S waves) is primarily from the first source, at 13 km. The shallow source (near 1 km) contributes little to the stations along the profile II. However, it does produce strong surface waves for the stations in the San Fernando Basin region and also contributes to the generation of surface waves in the Los Angeles Basin. This study suggests that the observed ground motions are indeed affected strongly by propagation paths along different structural provinces.

## II. Finite-Difference Synthetic Seismograms for SH Waves

by *J. Vidale, Don Helmberger and Rob Clayton*

### INTRODUCTION

The understanding of earthquake generated motions has improved significantly in recent years. This progress is due to the refinement of methods for generating synthetic seismograms in the attempt to replicate observed seismograms and the dramatic improvements in computers as well as an ever growing collection of observations. The synthetic seismogram incorporates our best guess about the earthquake source properties and the distortions caused by propagation through the Earth. Our knowledge of sources and earth structure is dependent on the accuracy and versatility of the method for synthetic seismogram generation.

The earth was first approximated by a wholespace; it then evolved to a halfspace, and it is currently a stack of homogeneous layers in which the number of layers is controlled by one's computer budget. In this paper, we relax some of these strong limitations by allowing dipping structure and introducing a procedure whereby 2-D finite difference (FD) calculations can be mapped into synthetic seismograms with the proper point source shear dislocation characteristics. This procedure has the advantage of allowing for arbitrary density and velocity fields in two dimensions.

This paper only treats SH waves (horizontally polarized shear waves) but the method may be extended to P-SV waves. We will begin by reviewing line source theory, which is the physical basis for the FD method. The similarity of the generalized ray theory (GRT) expressions for strike-slip and dip-slip types of

sources leads to identification of the vertical radiation patterns required for the line-source FD source. FD seismograms using these radiation patterns are seen to agree well with GRT seismograms. Finally, the utility of FD methods with the proposed mapping is shown for several applications.

## SOURCE REPRESENTATION

Consider a dislocation source which is situated below a layer as shown Figure 1. The displacement at the free surface can be obtained by summing generalized rays, after Helmberger and Malone (1975)

$$v(t) = \frac{M_0}{4\pi\rho_0}\frac{d}{dt}\left[\frac{d\,D(t)}{dt} * \sum_{j=1}^{2} A_{j+3}(\theta,\lambda,\delta)\, V_j(t)\right] \qquad (1)$$

where

$$V_j(t) = \sqrt{\frac{2}{r}}\frac{1}{\pi}\left[\frac{2}{\sqrt{t}} * \sum_{i=1}^{n}\left(\frac{p^{3/2}}{\eta_2} SH_j(p) \prod \frac{dp}{dt}\right)_i\right] \qquad (2)$$

and t is time in seconds, r is horizontal distance between source and receiver in km, n is the number of rays used to approximate the response, $M_0$ = moment in dyne-cm, $\rho_0$ = density in grams/cm$^3$ at source, D(t) = dislocation history across the fault element, and $\frac{d\,D(t)}{dt}$ = far-field time function. $A_4$ and $A_5$ contain the dependence on azimuth and mechanism and are

$$A_4 = \cos 2\theta \cos\lambda \sin\delta - \frac{1}{2}\sin 2\theta \sin\lambda \sin 2\delta \qquad (3a)$$

$$A_5 = -\sin\theta \cos\lambda \cos\delta - \cos\theta \sin\lambda \cos 2\delta \qquad (3b)$$

where $\theta$ = strike from the end of the fault, $\lambda$ = rake angle, and $\delta$ = dip angle. The fault orientation conventions are given in Figure 2.

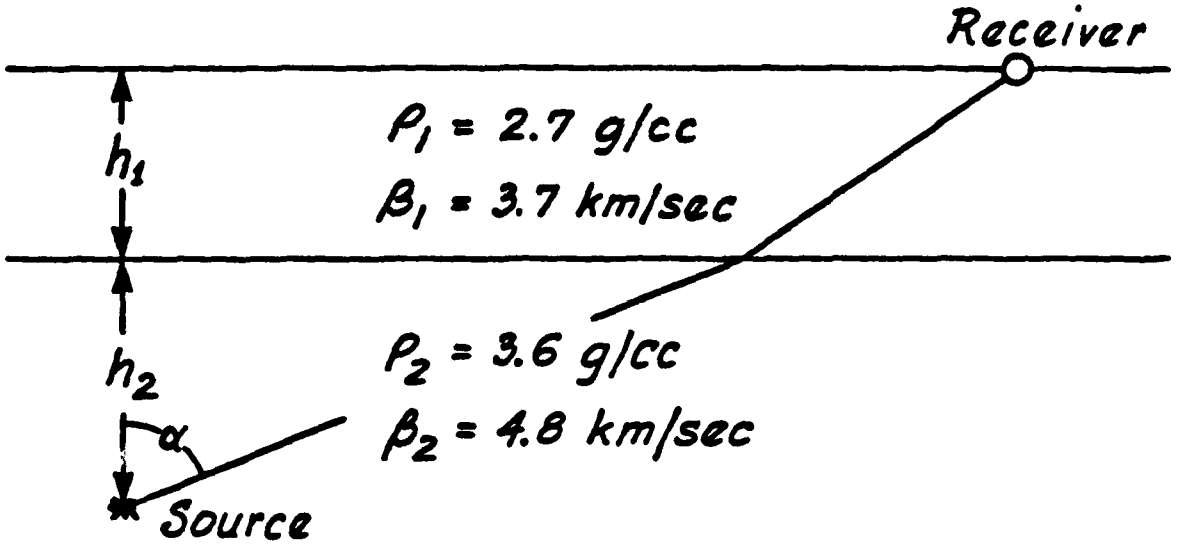


**Figure 1. Flat layer over a halfspace geometry with shear wave velocities and densities.**

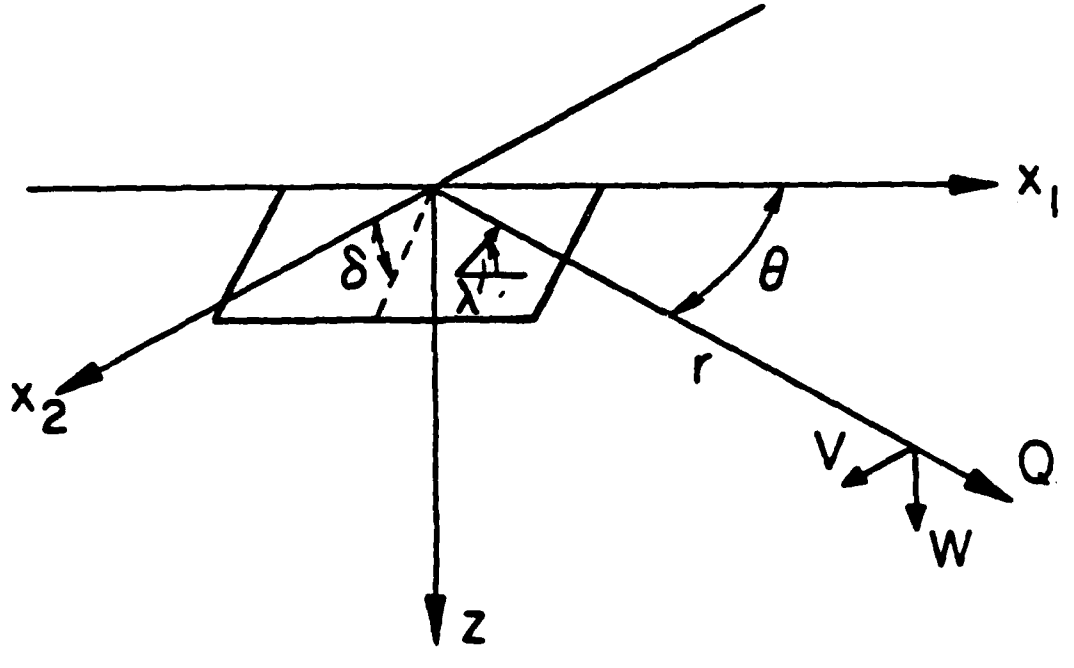


**Figure 2. Description of conventions for angles in mechanism and orientation for this paper.**

$$SH_1 = \frac{1}{\beta_0^2} \tag{4a}$$

and

$$SH_2 = \frac{-\varepsilon\,\eta}{\beta_0^2\,p} \tag{4b}$$

are the strike-slip and dip-slip vertical radiation patterns and $\beta_0$ is the shear wave velocity in km/sec at the source. $\varepsilon$ is -1 for receivers above the source, but +1 for receivers below the source. $\prod_i$ is the product of transmission and reflection coefficients for the $i^{th}$ ray, $p = \frac{\sin\alpha}{\beta}$ is the ray parameter, and

$$\eta_i = \left(\frac{1}{\beta_i^2} - p^2\right)^{1/2}$$

$$t_i = p\,r + \eta_2\,h_2 + \eta_1\,(2i - 1)\,h_1$$

and $\left(\frac{dp}{dt}\right)_i$ is determined from $t_i(p)$.

Note that $V_1(t)$ and $V_2(t)$ do not depend on azimuth or mechanism but contain only the vertical radiation patterns. This separation allows the two $V_j$'s to be constructed by equation (2) and the azimuthal pattern and mechanism to be calculated by equation (1).

If we allow $\beta_1 = \beta_2$, equation (2) simplifies for $t_r >> T$, where T is the source duration and $t_r = \frac{R}{\beta}$ to

$$V_1 = 2\,\frac{\sin\alpha}{\beta^3}\,\frac{H(t - t_r)}{R} \tag{5}$$

for a strike-slip fault and

$$V_2 = 2\,\frac{\cos\alpha}{\beta^3}\,\frac{H(t - t_r)}{R} \tag{6}$$

for a dip-slip fault where R is the source to receiver distance and $\alpha$ is the angle between the vertical and a line connecting the source and receiver as shown in Figure 2. Thus, the trigonometric functions specify the well-known radiation patterns. Substituting (5) into (1) and letting $\lambda = 0^0$ and $\delta = 90^0$ for the strike-slip case, we obtain

$$v(r,z,t) = \frac{M_0}{4\pi\rho_0} 2 F_0 \left( \frac{\sin\alpha}{\beta^3} \right) \cos 2\theta \frac{d\, D(t - t_\tau)}{dt} \frac{1}{\gamma R} \tag{7}$$

where the amplitude of the displacement is given in centimeters, $M_0$ in dyne-cm, $\rho_0$ in grams/cm$^3$ , $\beta$ in km/sec, R in km, and $F_0 = 10^{-20}$ for unit conversion and $\gamma = D(\infty)$ for strength normalization. We will express most of our results with $\frac{M_0}{4\pi\rho_0} F_0 = 1$ or for a moment of $M_0 = 4\pi\rho_0 \times 10^{20}$ dyne-cm.

As R and therefore $t_\tau$ becomes small, we need to improve our approximations by including a pseudo-near-field term, see Helmberger (1983)

$$V_1 = \frac{2}{\beta^2} \frac{1}{R} Re(p)\, Im\left( \frac{1}{\eta_\beta} \frac{dp}{dt} \right) \tag{8a}$$

which simplifies to

$$V_1 = \frac{2\, t\, \sin\alpha}{\beta^2} \frac{H(t - t_\tau)}{R} \frac{}{R} \tag{8b}$$

and

$$V_2 = \frac{2}{\beta^2} \frac{1}{R} Re(\eta)\, Im\left( \frac{1}{\eta_\beta} \frac{dp}{dt} \right) \tag{9a}$$

which simplifies to

$$V_2 = \frac{2\, t\, \cos\alpha}{\beta^2} \frac{H(t - t_\tau)}{R} \frac{}{R} \tag{9b}$$

These are not the complete near-field effects but only compatible with the asymptotic nature of the solution. If $\Psi$ were to include the exact near-field solution for the radiated SH waves, we would have to include the near-field contributions of P and SV as well, as described in Helmberger and Harkrider (1978).

The solution for a symmetric line source assuming the same geometry as displayed in Figure 1 becomes

$$\Phi(r,z,t) = \frac{d}{dt}[\, f(t) * \Psi \,] \tag{10}$$

$$\Psi = 2 \sum_{i=1}^{n} \left( \frac{\prod}{\eta_2} \frac{dp}{dt} \right)_i \tag{11}$$

with the same definitions given for expressions (1) and (2). A generalization of line source theory to include dipping structure is given by Hong and Helmberger (1977).

If we suppose $\beta_1 = \beta_2$ as for the point source discussed above, we obtain

$$\Psi = \frac{2\, H(t - \frac{R}{\beta})}{\sqrt{t^2 - \frac{R^2}{\beta^2}}} \tag{12}$$

where the factor of two is the free surface effect. Substituting (12) into (10), we obtain

$$\Phi(r,z,t) = \frac{2\, f(t - \frac{R}{\beta})}{\sqrt{t^2 - \frac{R^2}{\beta^2}}} \tag{13}$$

which is the well-known line source solution. By comparing expression (11) with (2) and the near-field effects just discussed, we can determine the constants and mapping required, namely let

$$V_j(t) = \frac{1}{\sqrt{t}} * \Phi_j \tag{14}$$

where $\Phi_j$ is the output of the FD code with the following source descriptions

$$\Phi_1 = \Phi_0 \left(\frac{\sin \alpha}{R}\right) t \frac{H(t - t_\tau)}{\sqrt{t^2 - \frac{R^2}{\beta^2}}} \tag{15a}$$

for the strike-slip orientation and

$$\Phi_2 = \Phi_0 \left(\frac{\cos \alpha}{R}\right) t \frac{H(t - t_\tau)}{\sqrt{t^2 - \frac{R^2}{\beta^2}}} \tag{15b}$$

for the dip-slip. The constant is

$$\Phi_0 = \beta^{-\alpha/2} \sqrt{\frac{2}{R}} \tag{16}$$

The point source seismograms due to shear dislocations are generated with equation (1) using the $V_j$ from equation (14) which use $\Phi_j$ from the FD code.

The separation of variables between the $V_j$'s and the $A_j$'s allows two different ways to use equation (1). If several synthetic seismograms are desired, one calculates both $V_j$'s from two FD runs and combines them with the appropriate $A_4$ and $A_6$ for each seismogram. If only one seismogram is desired, one can combine the $V_j$'s with the appropriate A's to create the source and only run the FD code once.

We will next discuss the FD method followed by comparisons of FD against the line source GRT results as given by equations (10) and (11), and followed by point source mapping comparisons and dipping GRT results.

## FINITE DIFFERENCE TECHNIQUES

The finite-difference (FD) SH code used is similar to the acoustic code described by Brown and Clayton (1977). The code is fourth-order for regions homogeneous in velocity and second-order for regions heterogeneous in velocity, see Alford et al, 1974, for definition and examples of order for FD codes. The fourth-order scheme is used to combat grid dispersion, which slows down the propagation of the higher frequency waves. Figure 3 shows the actual phase velocity divided by the nominal phase velocity plotted against period in seconds and wavelength in number of grid intervals. The line with solid circles indicates the phase velocity of the fourth-order FD algorithm used for homogeneous regions and the line with hollow circles indicates the phase velocity of the second-order algorithm used for heterogeneous regions. The fourth-order scheme allows propagation at approximately the correct velocity for energy with wavelengths down to five grid points, or one-half the limit of 10 points per wavelength of a second-order scheme. The second-order heterogeneous conditions are used because of the difficulty of deriving simple, stable fourth-order heterogeneous schemes. The second-order heterogeneous scheme is sufficiently accurate for the purposes of this paper and is faster.

Absorbing boundary conditions are imposed on the sides and the bottom of the FD grid as described by Clayton and Engquist (1980), and the top of the grid is made a free surface for SH waves (reflection coefficient = 1) by the method of Alterman and Karal (1968).

Several schemes for source insertion have been described in the literature. Imposing the displacement as a function of time either at one side or at the bottom of the box works if the source is too far from the receiver to be embedded in the box (see Boore, 1972, for example). A simpler approach imposes an initial displacement in a source region for the first two time steps and leaves the grid source free for the remaining time steps (Alford et al, 1974). A third method

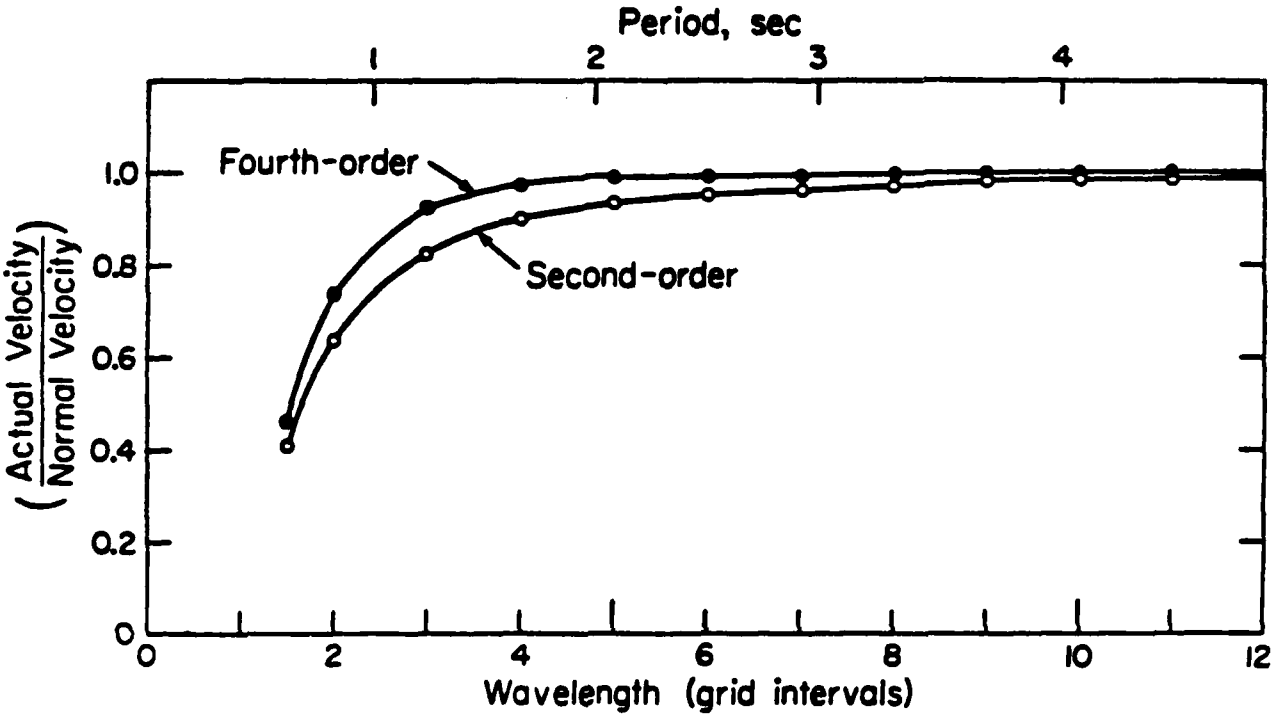


**Figure 3. Phase velocity divided by nominal velocity plotted against wavelength measured in grid spaces on the bottom and period in seconds on the top.**

commonly used is described in Alterman and Karal (1968). Essentially, it solves the wave propagation twice in the source region, once imposing the source and once without a source, and combines the results so that the source box does not act as a rigid reflector. This method has the advantage that the source may be "left on" for as long as desired. We use the method of Alterman and Karal (1968), except that fourth instead of second order boundary conditions are used to match the source region with the surrounding region. This method is used because we desire a source within the grid and the wavelengths of interest would compel unacceptably large source boxs with the method of Alford et al (1974). A 9 by 9 grid point source is used, which is necessarily homogeneous for our source generation program.

Figure 4 illustrates the various sources. The frames in Figure 4 are snapshots of displacements throughout a small grid at a given time. The left frames are the displacements 25 timesteps into the calculation or when the transient wave is halfway to the edges and the right frames are after 50 timesteps or when the transient wave has propagated almost to the edge of the box. The amplitude scale for each plot is different. Positive displacements are filled in with black, but negative displacements are difficult to discern. All three types of sources have a transient wave which moves outward, but the sin $\theta$ and cos $\theta$ sources also have a two-lobed displacement pattern which is permanent. This permanent displacement is analogous to permanent deformation caused by movement on a fault.

The source for Figures 5 through 8 is symmetric and generated analytically by convolving an excitation function with the impulse response for a line source which is given in expression 13. Figures 9 through 12 use the dislocation sources given in Figure 4. These source functions introduce permanent displacement to the source area, just as would be expected from an actual

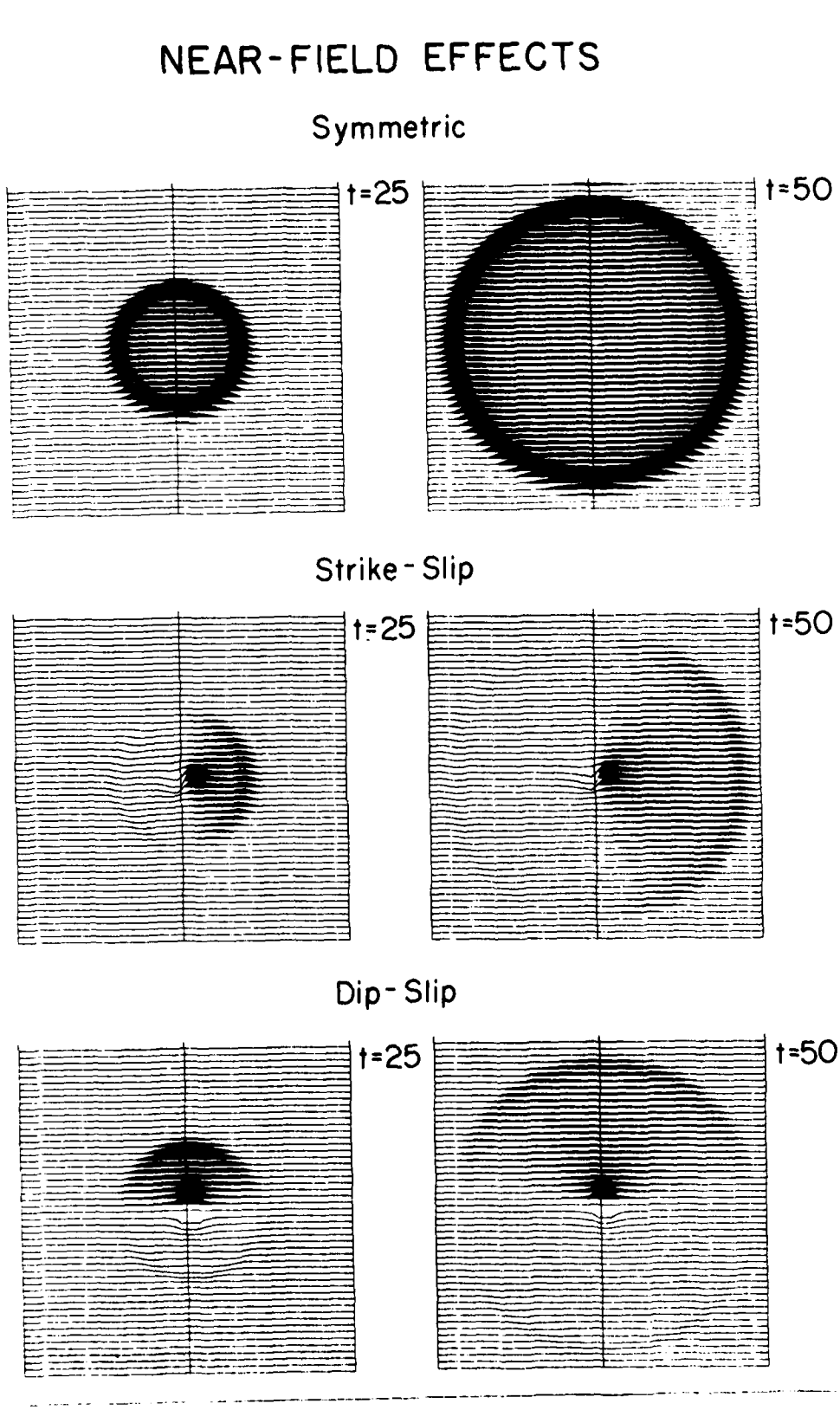


**Figure 4. Snapshots of displacements for the symmetric source, the sin $\theta$ mechanism source, and the cos $\theta$ mechanism source. The left frames show displacements after 25 timesteps, the right after 50. Amplitude scales are not uniform. Positive but not negative displacements are filled in with black.**

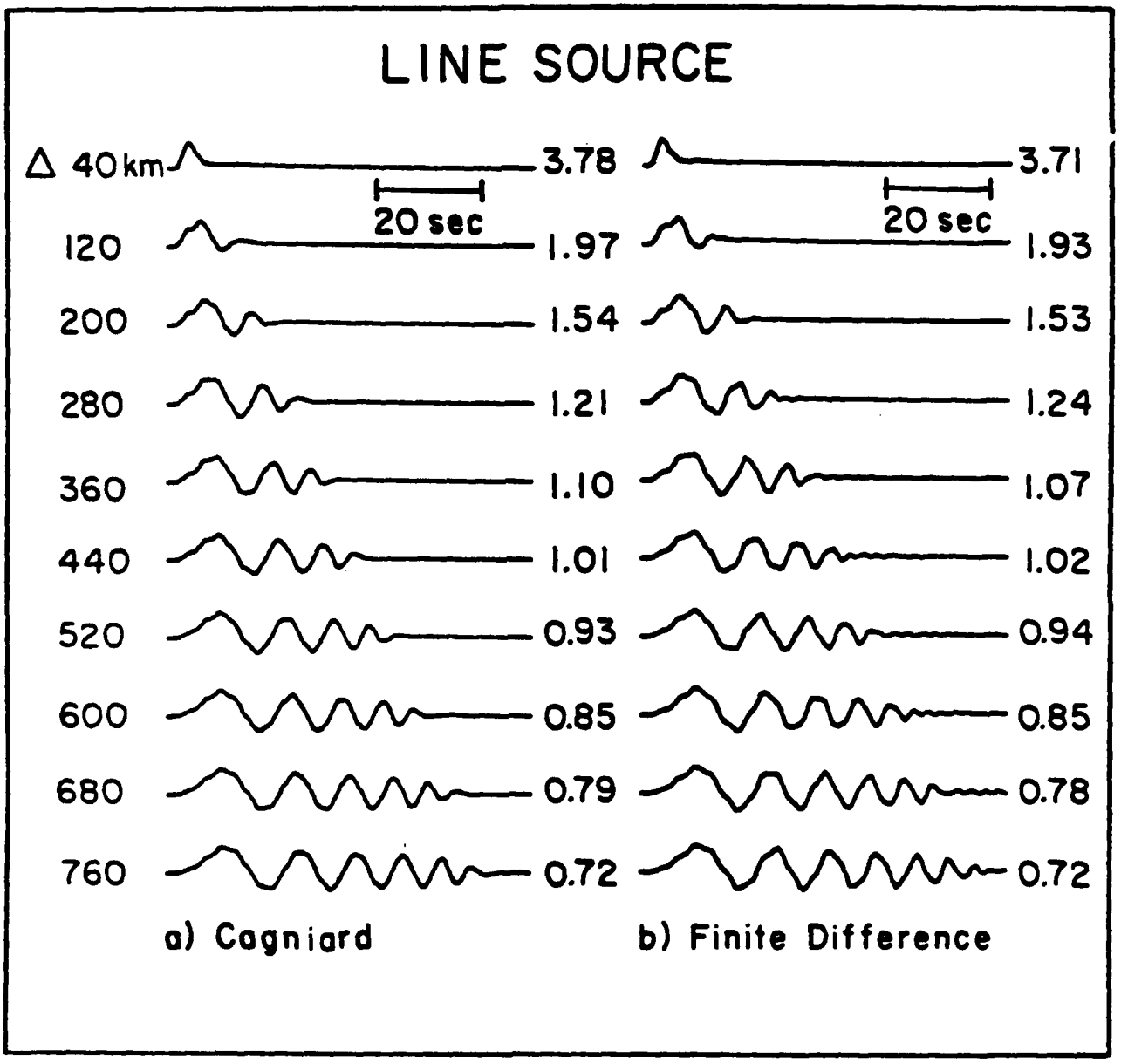


Figure 5. Comparison of the line source synthetic seismograms generated by the GRT and FD methods. Results are for a 9 km thick layer over a halfspace. The source is 9 km below the layer and the receivers are on the surface and range from 40 to 760 km in horizontal distance from the source. Both sets of seismograms are convolved with a trapezoidal time function. The amplitudes are absolute.

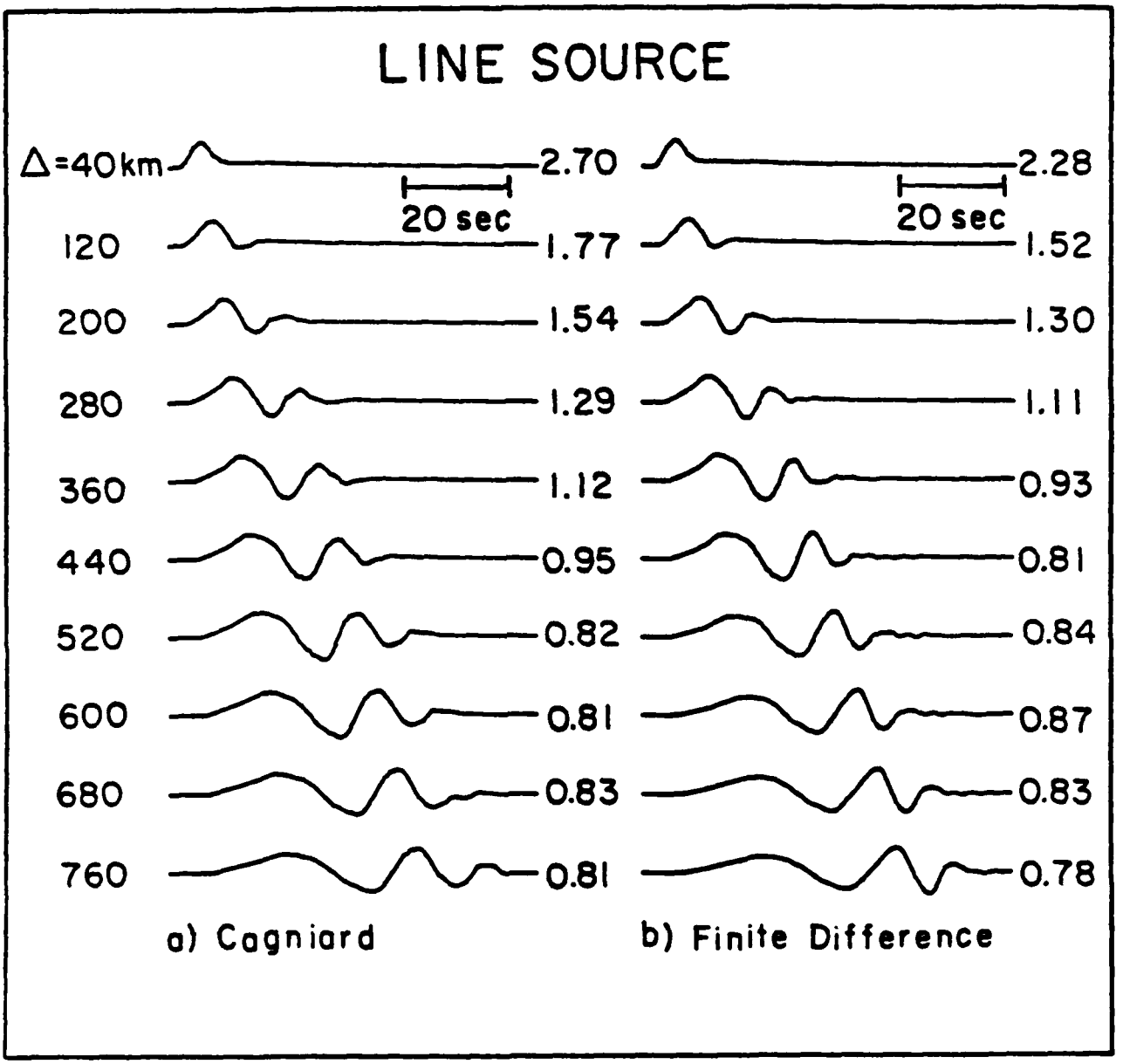


Figure 6. Comparison of the line source synthetic seismograms generated by the GRT and FD methods. Results are for a 9 km thick layer over a halfspace. Results are for a layer which ranges in thickness from 9 km above the source to 45 km at a range of 900 km.

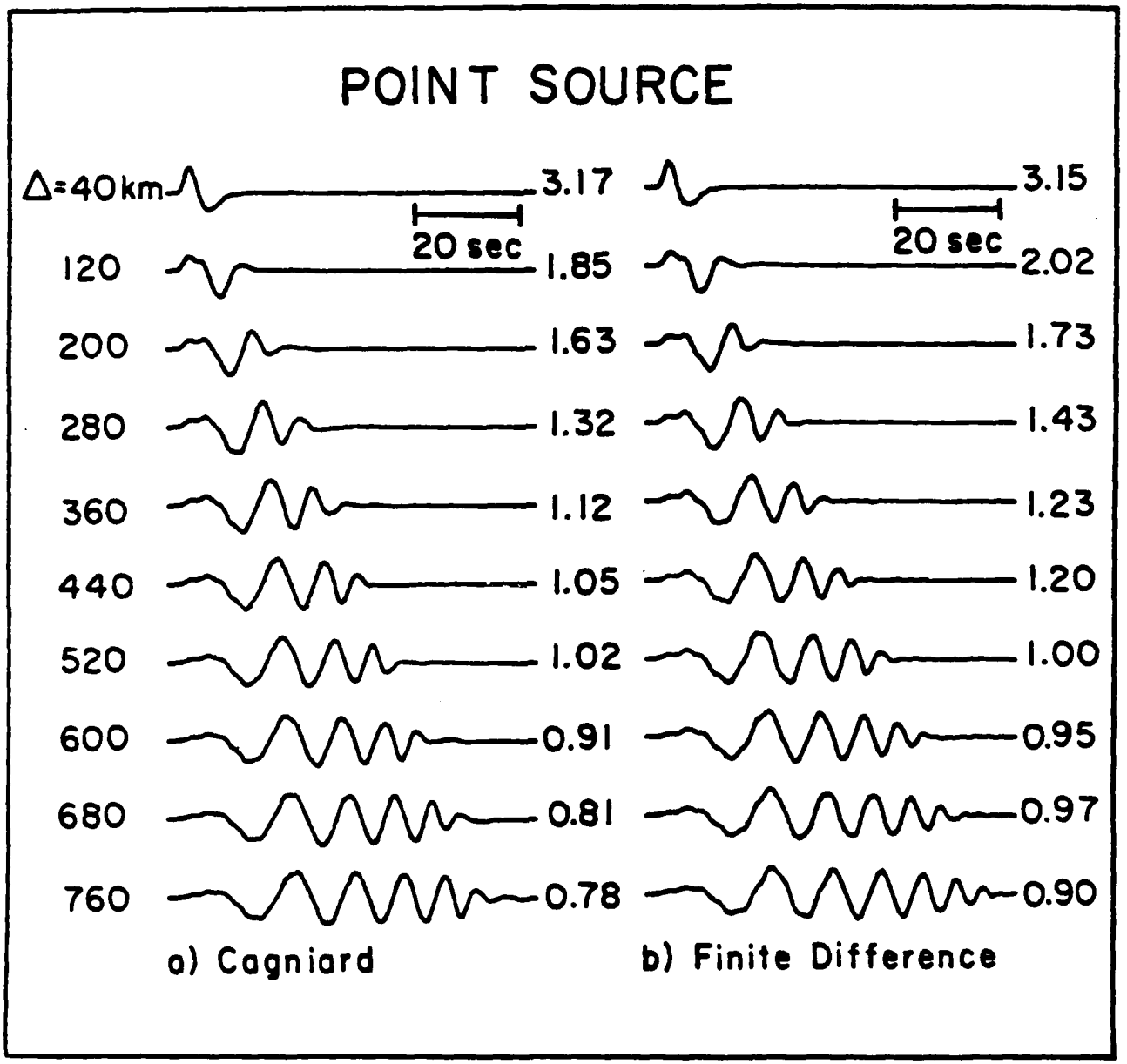


Figure 7. Comparison of the point source synthetic seismograms generated by the GRT and FD methods for the same flat-layer geometry as is used for Figure 5. Amplitudes are absolute and may be scaled to moment.

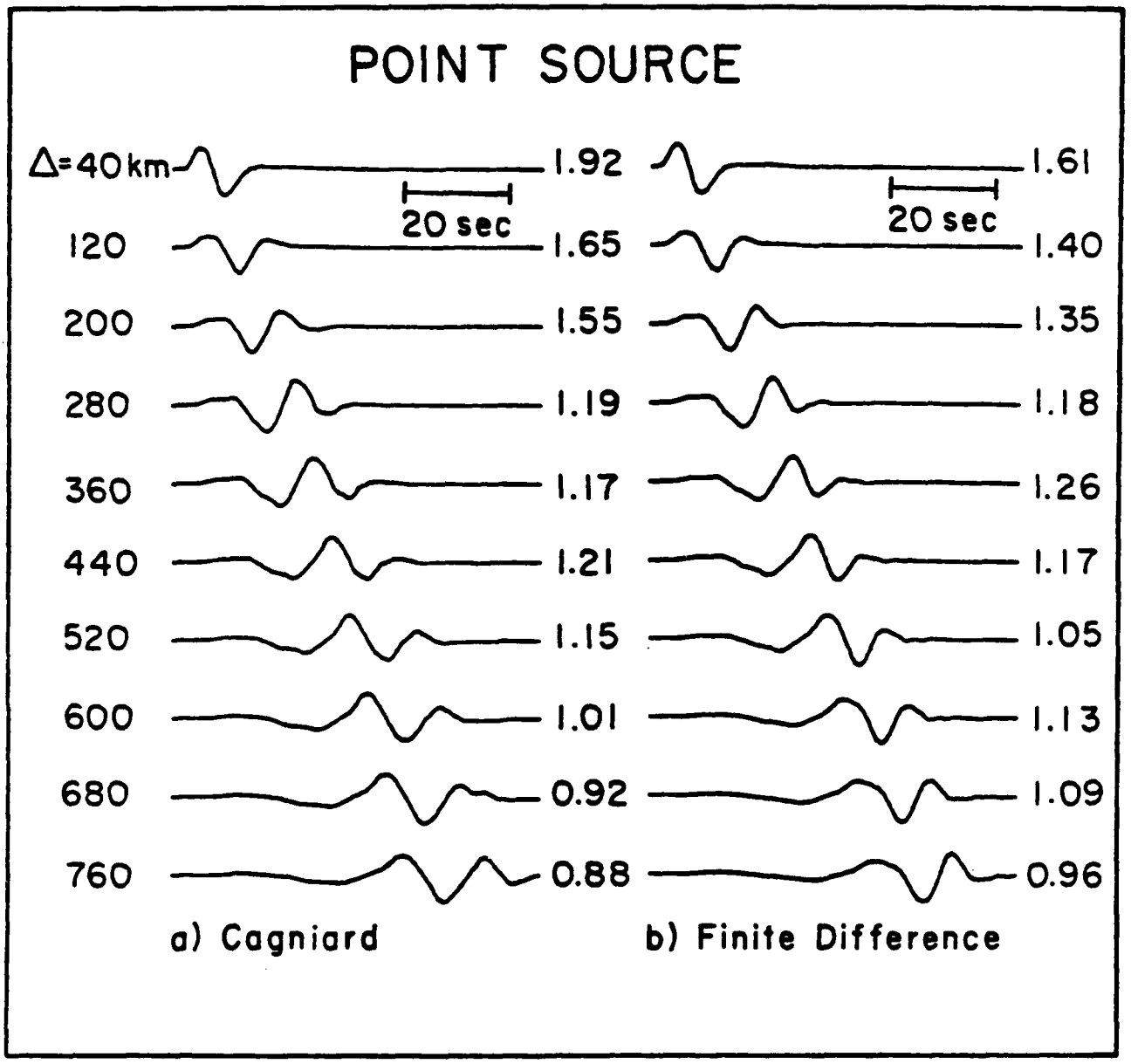


Figure 8. Comparison of the point source synthetic seismograms generated by the GRT and FD methods for the same dipping-layer geometry as is used for Figure 6.

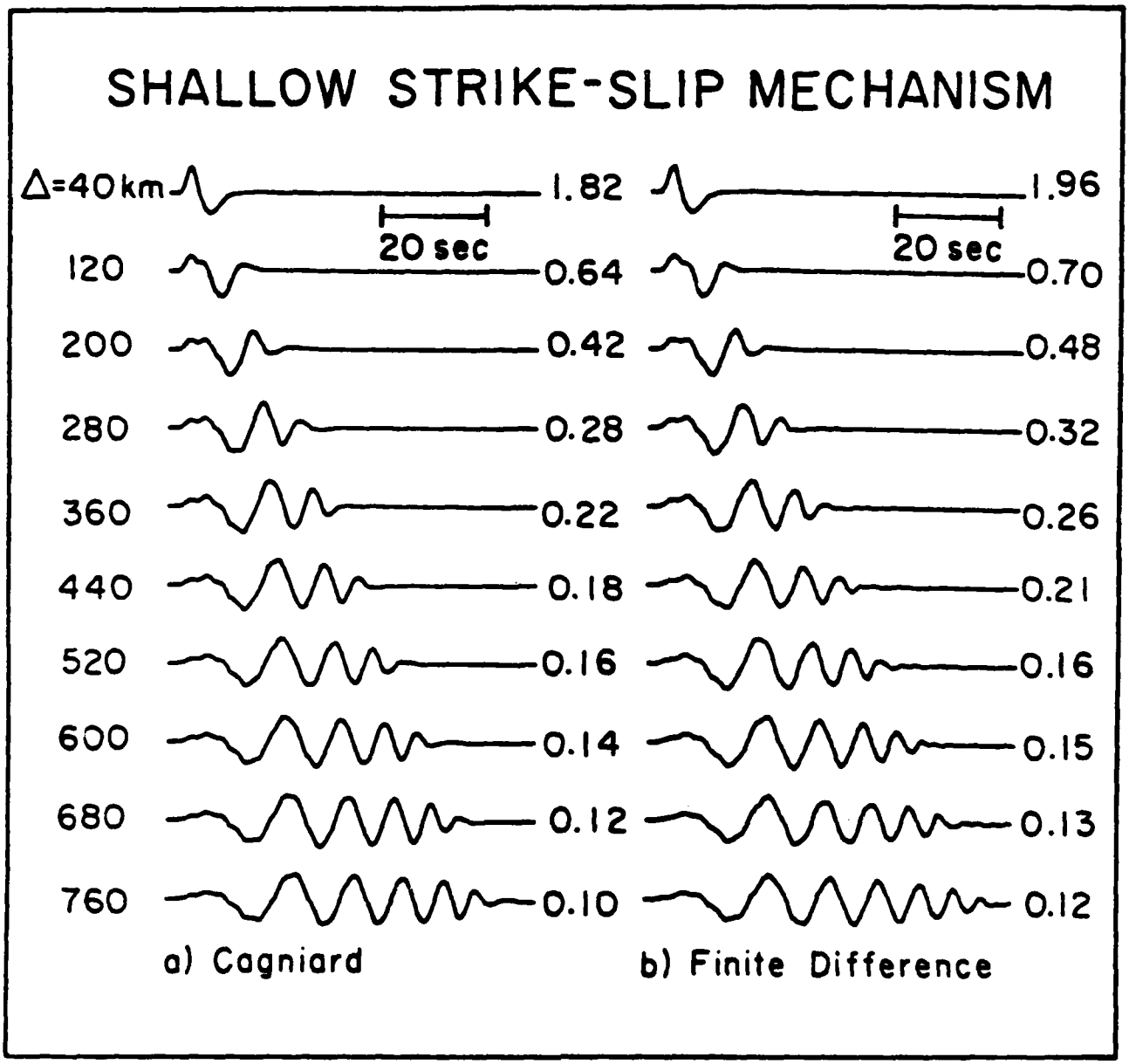


Figure 9. Comparison of the point source cos $\theta$ mechanism synthetic seismograms generated by the GRT and FD methods for the same flat-layer geometry as is used for Figure 5.

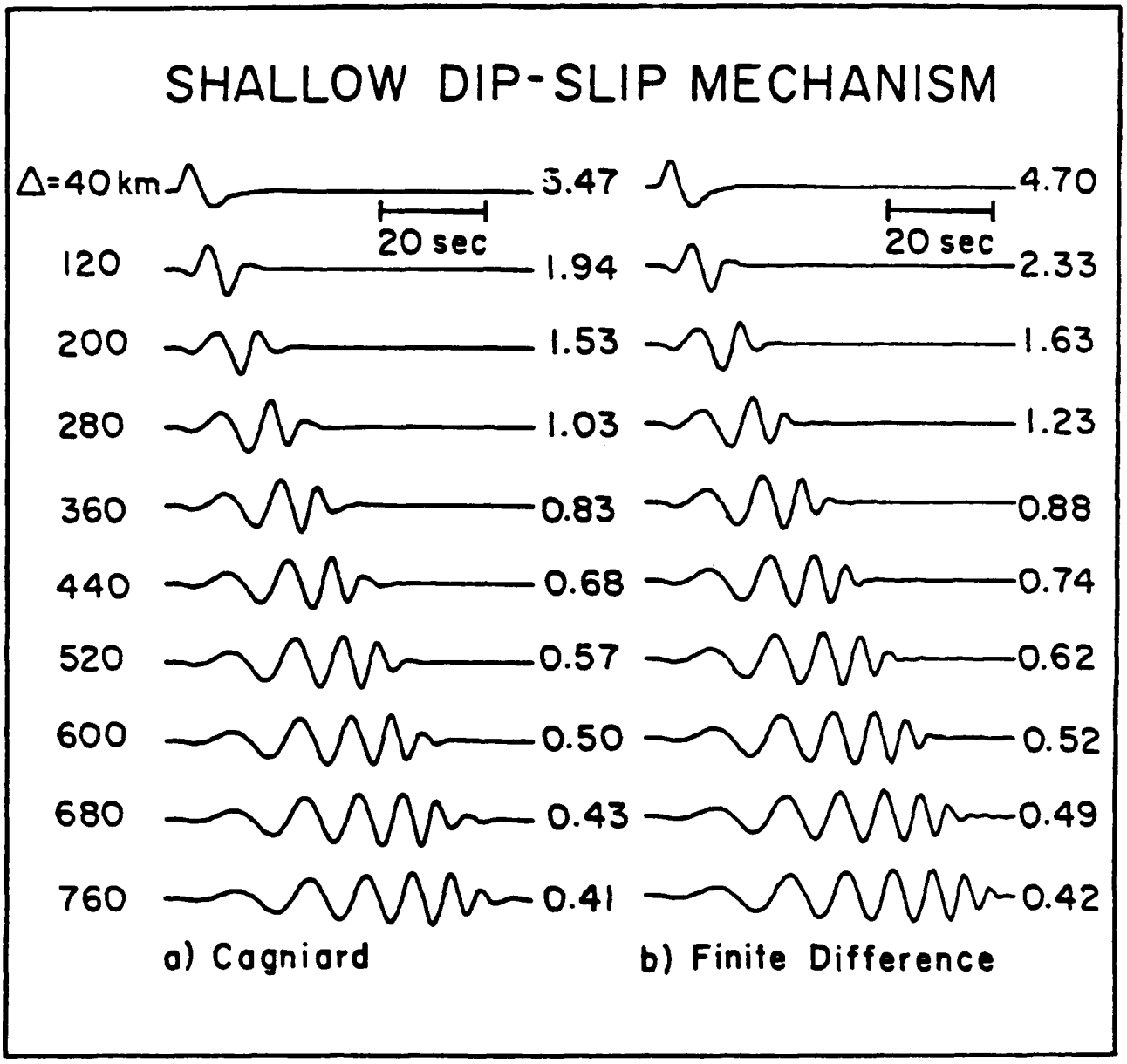


Figure 10. Comparison of the point source sin $\theta$ mechanism synthetic seismograms generated by the GRT and FD methods for the same flat-layer geometry as is used for Figure 5.

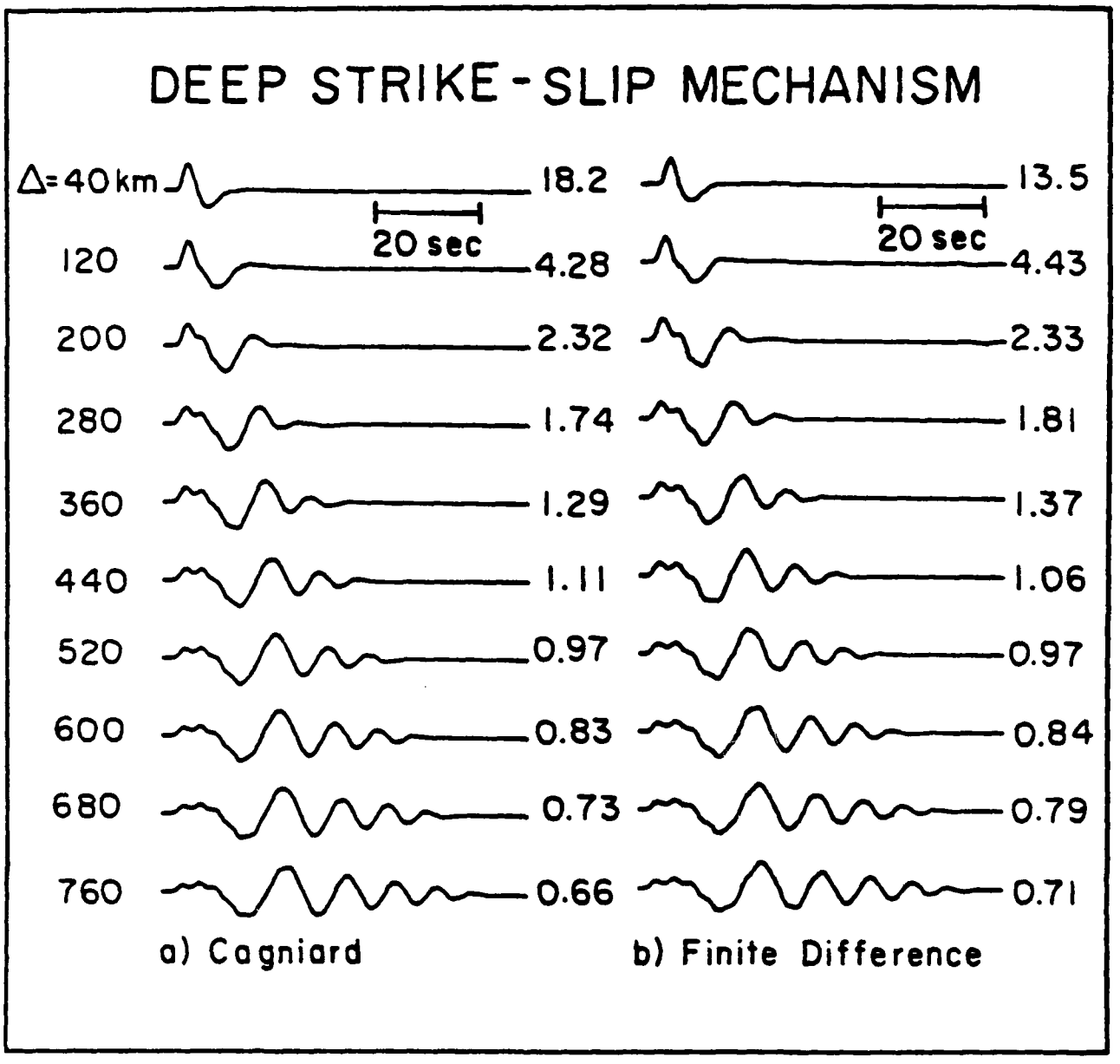


Figure 11. Comparison of the point source cos $\theta$ mechanism synthetic seismograms generated by the GRT and FD methods. Results are for the same flat-layer geometry as is used for Figure 5 except that the source is 25 instead of 9 km below the layer.

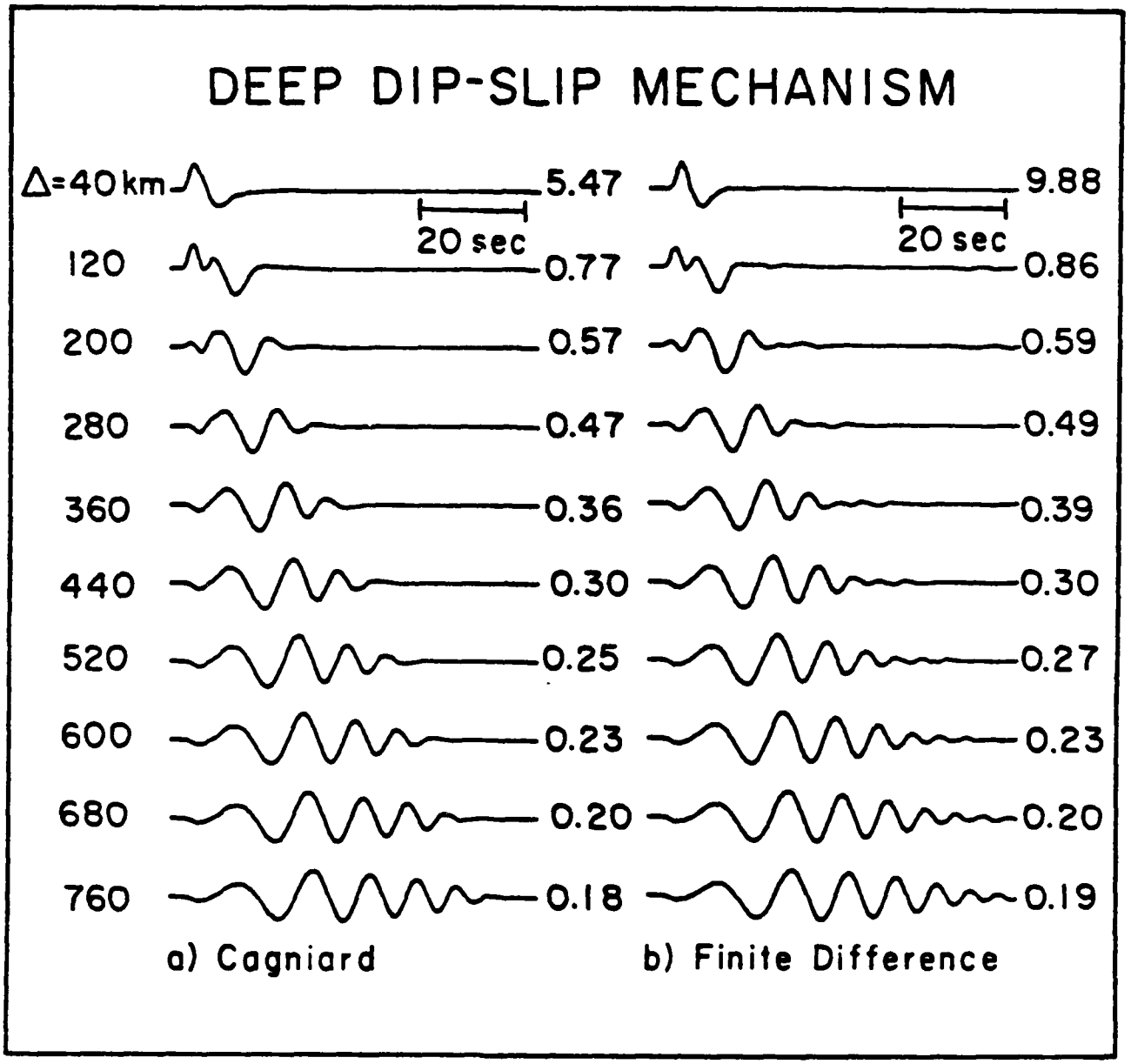


Figure 12. Comparison of the point source sin $\theta$ mechanism synthetic seismograms generated by the GRT and FD methods. Results are for the same flat-layer geometry as is used for Figure 5 except that the source is 25 instead of 9 km below the layer.

dislocation. For the line source, the permanent displacement falls off with distance as $r^{-1}$, while the transient displacement falls off as $r^{-1/2}$.

Line source seismograms are described above, but point source seismograms are desired. Line source seismograms may be transformed to point source seismograms by equation 14 as described above. A linear sum of the two sets of point source seismograms can be used to make seismograms for any strike, dip, and rake earthquake mechanism for a given velocity and density structure as given by equation 1.

We use a trapezoid of 3 second duration with 1 second rise time and 1 second fall time as an excitation function for the flat layer models. A trapezoid of 6 second duration with 2 second rise and fall times is used for the dipping layer models. The trapezoidal time functions filter out frequencies which would disperse in the grid and may be thought of as source time functions for the synthetic "shear explosions" and earthquakes as is common in modeling earthquake records (Langston and Helmberger, 1975).

A symmetric point or line source is easily grasped intuitively if the state variable is pressure in an acoustic problem, but a symmetric SH source is more difficult. A symmetric SH line source may be visualized as being due to a tug on the line source. A symmetric SH point source, however, must simply be considered to have the same SH amplitude and sign for every take-off angle and azimuth.

## COMPARISON

A model with one layer over a halfspace which represents simple oceanic lithosphere is chosen to compare the FD code with the flat layer GRT code which has been well-tested (see Apsel and Luco, 1984, for example). The geometry is shown in Figure 2. The crust has $h_1$ of 9 km with a density $\rho_1$ of 2.7 g/cm$^3$ and

shear wave velocity $\beta_1$ of 3.7 km/sec, and the underlying upper mantle has $\rho_2$ of 3.6 g/cm$^3$ and $\beta_2$ of 4.8 km/sec. The source is placed 18 km below the surface, or $h_2$ = 9 km.

Receivers in the plots in Figures 5 through 12 are positioned on the surface at lateral distances of 40 to 760 km from the source. These plots are reduced by a 4.8 km/sec velocity.

Figure 5 contains synthetic seismograms for the line source problem with symmetric source. Results from the GRT code are shown with in Figure 5a and results from the FD code are shown in Figure 5b, where the agreement is seen to be excellent.

Amplitudes differ between the two sets of synthetics by no more than 3%, and the detailed waveforms are nearly identical. Even the highest frequencies shown agree well for the first portion of each seismogram. The later portion of the FD seismograms show some contamination by dispersed high frequency energy. This agreement is consistent with Figure 3, which shows that energy with periods above two seconds for the homogeneous regions and four seconds for the heterogeneous regions should be propagated correctly. The discrepancies between the traces are high frequency and small.

A dipping layer over a halfspace model which represents a simple ocean-continent transition zone is chosen to compare the FD code with the dipping-layer GRT code. The crust is again 9 km thick directly above the source and again the source is 9 km below the crust. The thickness of the crust increases linearly to 45 km at a range of 900 km. The same geometry of receivers is used as in the previous case.

The results for a symmetric source from the FD code are shown in Figure 6a and from the dipping layer GRT code in Figure 6b. The higher frequencies have worse agreement than in the flat layer case, so the excitation function used is a

six second trapezoid with two second rise and fall times. The amplitude of the FD seismograms are 3 to 4% greater for the outer 4 receivers, but 12 to 18% less for the inner six. The discrepancies between Figures 6a and 6b may be due to either code. The most likely problems are dispersion in the FD code as mentioned above or the necessary approximation of a dipping layer by a series of steps in the FD method. The GRT code does not consider rays which bounce first away from the receivers before changing direction due to the dip in the layer and travel to the receivers. The amplitude of these rays is expected to be negligible, however. For the lower frequencies and the first part of the waveform in which we are primarily interested, the agreement is excellent.

The point source synthetics fare equally well. They are generated by equation 14, described above. The synthetics are convolved with the long-period WWSSN instrument response. The longest and shortest period energy is attenuated in transforming the line source seismograms to point source seismograms, primarily due to the instrument response. Figure 7a shows traces generated by the point-source, flat-layer GRT program and Figure 7b shows the traces in Figure 5b after the transformation described above. Similarly, Figure 8a shows traces generated by the point-source, dipping-layer GRT program and Figure 8b shows the traces in Figure 6b after transformation. The agreement in waveform is excellent for the flat layer case and good for the dipping layer case. The amplitudes agree to within 20% for all cases.

The next question is whether the FD seismograms with mechanisms inserted agree with their GRT equivalents. For Figures 9 and 10 the flat layer model described above is used. Figure 9 shows traces for the cos $\theta$ radiation pattern, with the GRT-generated seismograms in Figure 9a and the FD seismograms in Figure 9b. Similarly, Figure 10 shows traces for the sin $\theta$ radiation pattern. As a further check, a source 25 instead of 9 km below the layer is used

in Figures 11 and 12. The agreement in waveform is excellent, and again the amplitudes agree to within 20%. The exceptions are the seismograms recorded 40 km away for the source 34 km deep, whose amplitudes are substantially in error. It appears that the discrepancy at $\Delta = 40$ km is caused primarily in matching high frequency content between the two methods. For instance, in figure 9 the GRT appears shorter period whereas in figure 10 the FD is shorter period. These features are probably caused by the rather delicate interference between the direct wave and first multiple. The interface at the bottom of the layer is actually smoothed in the DF code and for angles of incidence less than critical angle we can expect a longer period reflection than for GRT responses. Since we are primarily interested in long range propagation in this mapping, we can ignore the sharpness of the crust-mantle transition which is built into the FD code in this situation.

## THE EFFECTS OF THE OCEAN-CONTINENT TRANSITION ON LOVE WAVES

If we are to understand the difference between the crust and upper mantle under oceans and continents, it is important to know the geometry of the transition zones. The sparsity of ocean-bottom seismometers and the relative quiescence of passive margins precludes direct travel-time inversion for velocity structure. Multichannel seismic arrays have good resolution, but deal primarily with P-waves and can only penetrate the sedimentary column and occasionally locate the Moho discontinuity (e.g. Talwani et al, 1982, and Avedik et al, 1982). Surface wave dispersion is often used to examine velocity structure, but most methods of surface wave dispersion analysis require either flat- or dipping-layered models. Velocity structure is known not to follow either flat- or dipping-layered geometries near ocean-continent boundaries.

The FD method allows more general models to be incorporated in synthetic seismogram generation, as described by Drake (1972), Drake and Bolt (1980) and Martel (1980). Such studies are two-dimensional, however, and are more complicated than the FD method described in this paper. Some three-dimensional finite-element models have been investigated by Gregersen and Alsop (1974) and Schlue (1981), but these models are not very realistic.

Several recent papers use approaches similar in some ways to ours. Fuyuki and Matsumoto (1980) use a two-dimensional P-SV FD scheme to investigate the effect of a trench on Rayleigh wave propagation. Stevens (1983) investigates the effect on seismic sections of bump on the seafloor with a three-dimensional P-SV FD code which assumes cylindrical symmetry. Kelly (1983) investigates the effect of near-surface geological features on the propagation of Love waves with a two-dimensional SH FD code.

In this section, the effect of differing ocean-continent transition geometry on Love wave waveforms is examined. Figure 13 shows the three geometries used to generate synthetic seismograms. In all cases, the upper layer has a density of 2.7 g/cm$^3$ and shear wave velocity of 3.7 km/sec and the lower layer has a density of 3.6 g/cm$^3$ and shear wave velocity of 4.8 km/sec. Symmetric shear sources are used; these create seismograms which are indistinguishable from strike-slip mechanisms for these ranges. The seismograms for the geometries shown in Figures 13a, 13b, and 13c are presented in Figures 14a, 14b, and 14c, respectively.

The seismograms for different geometries are distinguishable by waveform and timing but not by amplitude in synthetic seismograms. The differences in amplitude are of a similar magnitude to the errors noted above and are not clearly systematic. The waveforms at the first 4 receivers, $\delta$ = 40, 120, 200, and 280 km are identical because the structure between the source and receiver is

# OCEAN-CONTINENT TRANSITION GEOMETRIES

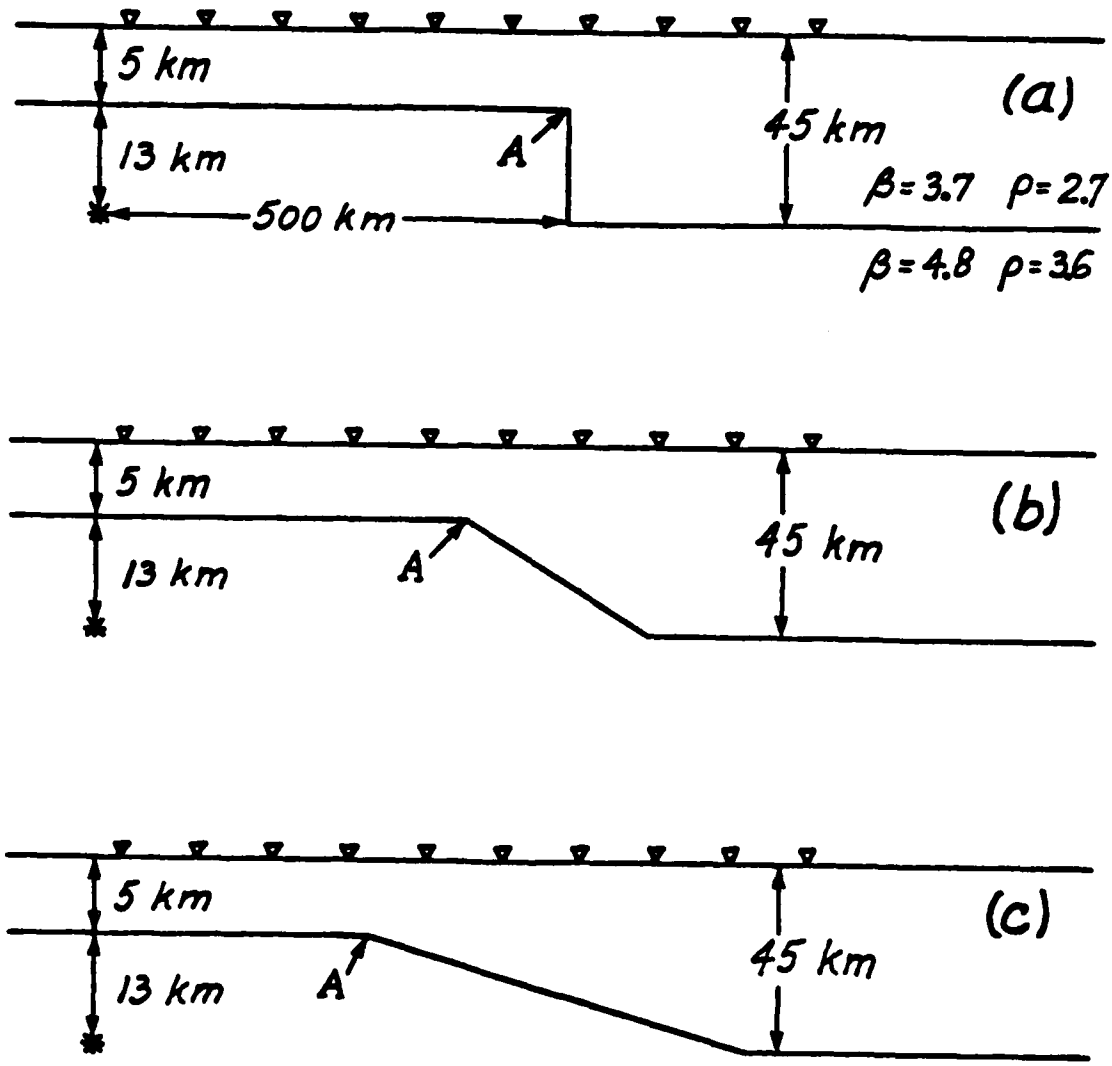


Figure 13. Shown are the three geometries which are used to generate the synthetic seismograms in Figures 14a, 14b and 14c. The stars indicate sources and the triangles indicate receivers. The crust has $\beta$ = 3.7 km/sec and $\rho$ = 2.7 g/cc and the uppermost mantle has $\beta$ = 4.8 km/sec and $\rho$ = 3.2 g/cc. The crustal thickness in each model varies from 5 km on the left to 45 km on the right.

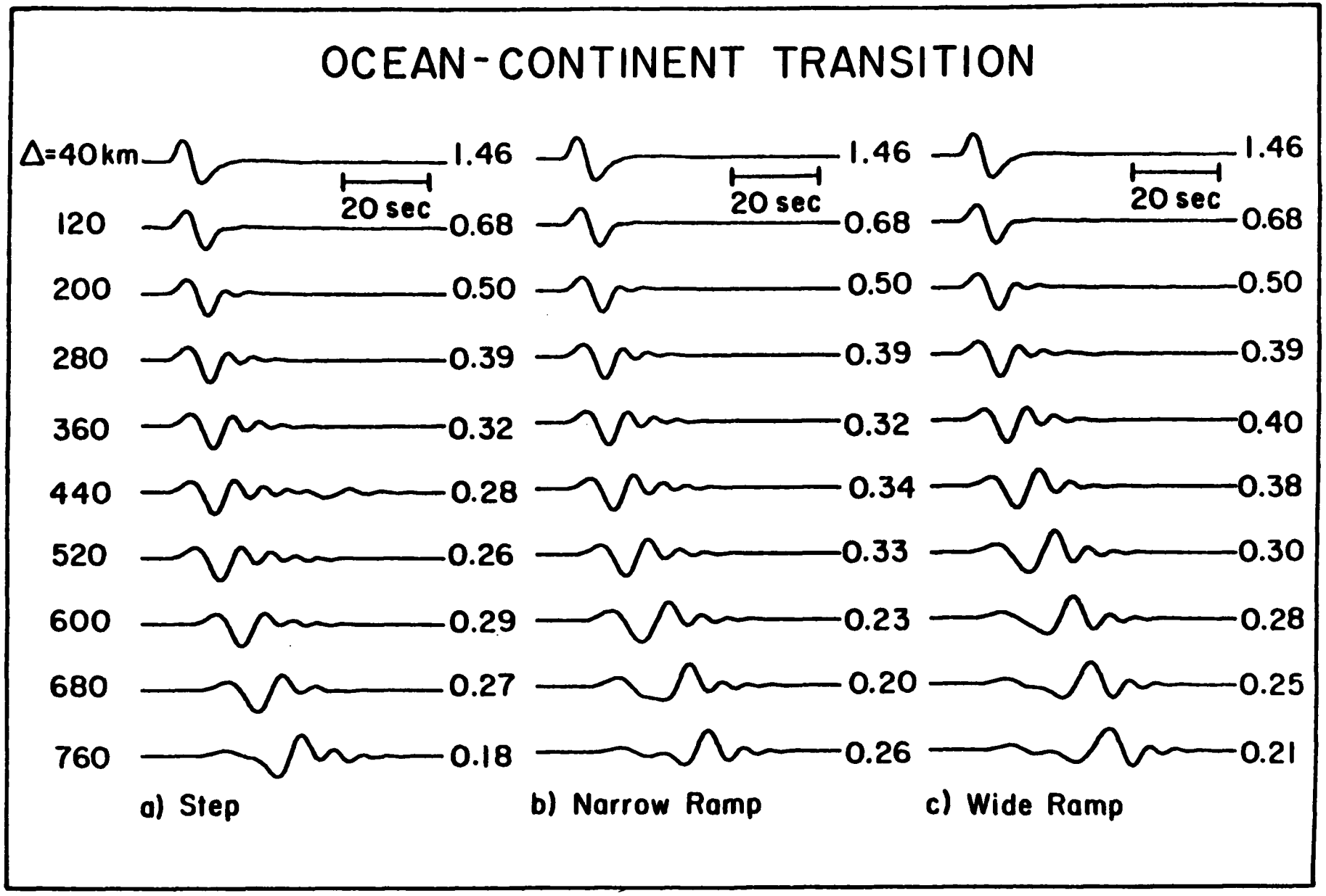


**Figure 14.** Suites of synthetic seismograms are shown for the 3 geometries depicted in Figure 13. The seismograms correspond to distances which range from 40 to 760 km. Amplitudes are absolute and may be converted to displacements when an earthquake moment is specified.

identical. The seismograms recorded directly above the transition zone at $\delta$ = 360, 440, and 520 km are very similar. The furthest seismograms recorded at $\delta$ = 600, 680, and 760 km are the most distinguishable. This pattern is fortunate because most of the available data is, of course, recorded on the continents. The energy arrives slightly later in the wide ramp model than in the narrow ramp model which in turn is slightly slower than in the step model. This trend may be due to energy entering the crust at points A in Figure 13. The slow crustal velocity then results in the differential delay mentioned above.

It has been noticed that observations are more long-period than synthetic seismograms constructed with impulsive sources. This effect may be due to drawn-out smooth earthquake source time functions or it may be due to Q (attenuation), which damps higher frequencies preferentially. This effect means that the longer period shape of the sections are the most helpful in the modeling of actual seismograms. Grand and Helmberger (1983) find empirically that the average crustal thickness between source and receiver seems to determine the shape of the long-period front of the seismogram. If this idea works, then the front of the seismograms at $\delta$ = 680 and 760 km should be similar. They are not identical, but the leading portion of the $\delta$ = 760 km seismograms for the two ramp geometries are very similar. If this idea proves usable, then one could determine the average thickness of the crust from the front of the seismogram and more detailed information about the crust-mantle transition from the later portion of the seismogram, which is perhaps more difficult to model.

## REFERENCES

Alford, R.M., K.R. Kelley and D.M. Boore, 1974. Accuracy of finite-difference modeling of the acoustic wave equation; Geophysics **39**: 834-842.

Alterman, Z., and F.C. Karal, 1968. Propagation of elastic waves is layered media by finite difference methods; Bull.Seism.Soc.Am., **58**: 367-398.

Apsel, R.J. and J.E. Luco, 1983. On the Green's functions for a layered halfspace; Bull.Seism.Soc.Am., **73**: 909-9??.

Avedik, F., A.L. Camus, A. Ginsburg, L. Montadert, D.G. Roberts, and R.B. Whitmarsh, 1982. A seismic and reflection study of the continent- ocean transition beneath the north Biscay margin; Phil.Trans.R.Soc.Lond.A, **305**: 5-25.

Boore, D.M., 1972. Finite difference methods for seismic wave propagation in heterogeneous materials, in Methods of computational physics, v. **2**: B. Alder, S. Fernbach, and M. Rotenberg, Eds., New York, Academic Press, 1-37.

Boore, D.M., K.L. Larner, and K. Aki, 1971. Comparison of two independent methods for the solution of wave scattering problems: response of a sedimentary basin to vertically incident SH waves; J.Geophys.Res., **76**: 558-569.

Clayton, R.W., and B. Engquist, 1980. Absorbing boundary conditions for wave equation migration; Geophysics, **45**: 895-904.

Drake, L.A., 1972. Love and Rayleigh waves in nonhorizontally layered media; Bull.Seism.Soc.Am., **62**: 1241-1258.

Drake, L.A., and B.A. Bolt, 1980. Love waves normally incident at a continental boundary; Bull.Seism.Soc.Am., **70**: 1103-1123.

Drake, L.A., and A.K. Mal, 1972. Love and Rayleigh waves in the San Fernando Valley; Bull.Seism.Soc.Am., **62**: 1673-1690.

Fuyuki, M., and Y. Matsumoto, 1980. Finite difference analysis of Rayleigh wave scattering at a trench; Bull.Seism.Soc.Am., **70**: 2051-2069.

Gregersen, S., and L.E. Alsop, 1974. Amplitudes of horizontally refracted Love waves; Bull.Seism.Soc.Am., **64**: 535-553.

Hanks, T.C., 1975. Strong ground motion of the San Fernando, California, Earthquake: ground displacements; Bull.Seism.Soc.Am., **65**: 193-225.

Heaton, T.H., 1982. The 1971 San Fernando earthquake: a double event? Bull.Seism.Soc.Am., **72**: 2037-2062.

Helmberger, D.V., and D.G. Harkrider, 1978. Modeling earthquakes with generalized ray theory, in ModernProblemsinElasticWavePropagation, edited by J. Miklovitch and J.D. Achenbach, 499-518, John Wiley, New York.

Helmberger D.V., and S.D. Malone, 1975. Modeling local earthquakes as shear dislocations in a layered half space, J.Geophys.Res., **80**: 4881-4888.

Hong, T.L., and D.V. Helmberger, 1977. Generalized ray theory for dipping structure, Bull.Seism.Soc.Am., **67**: 995-1008.

Kelly, K.R., R.W. Ward, S. Treitel, and R.M. Alford, 1976. Synthetic seismograms: a finite-difference approach; Geophysics, **41**: 2-27.

Langston, C.A., and D.V. Helmberger, 1975. A procedure for modeling shallow dislocation sources; Geophys.J.R.astr.Soc., **42**: 117-130.

Martel, L., 1980. Love wave propagation across a step by finite elements and spatial filtering; Geophys.J.R.astr.Soc., **61**: 659-677.

McCowan, D.W., P. Glover, S.S. Alexander, 1977. A static and dynamic finite element analysis of the 1971 San Fernando, California, earthquake; Geophys.J.R.astr.Soc., **48**: 163-185.

Schlue, J.W., 1981. Seismic surface wave propagation in three-dimensional finite-element structures; Bull.Seism.Soc.Am., **71**: 1003-1010.

Stephen, R.A., 1983. A comparison of finite difference and reflectivity

seismograms for marine models; Geophys.J.R.astr.Soc., 72: 39-57.

Talwani, M., P. Stoffa, P. Buhl, C. Windisch, and J.B. Diebold, 1982. Seismic multichannel towed arrays in the exploration of the oceanic crust; Tectonophysics, 81: 273-300.

# III. Array Analysis of the Ground Motions from the 1971 San Fernando California Earthquake

by Hsui-Lin Liu

## Introduction

An important new field of strong ground motion research is modeling of an earthquake source and the associated wave propagation in a deterministic way. This type of modeling has significantly increased our understanding of the longer-period parts of strong ground motions. However, a proper model is often difficult to obtain. An accurate characterization of the wave phenomenon, ( e.g., wave types, coherent phase velocities, propagation direction and the wave variability ) is essential to evaluate the validity of the models.

Hanks ( 1975 ) analyzed the ground displacements from the 1971 San Fernando strong-motion data and found strong coherence appeared in the longer-period waves. He also identified direct shear phases and subsequent surface waves at certain ranges. However, a deterministic source model for the 1971 San Fernando event is still uncertain as pointed out by Heaton ( 1982 ). Heaton constructed models consisting of finite faults within a half-space to explain waveforms observed at 5 strong-motion stations as well as long-period teleseismic body waveforms. His preferred finite source model implies a fairly complex double source earthquake, with two events of approximately equal size and separated by about 4 seconds. However, modeling of this type is limited by our incomplete knowledge of the strong motions propagating through the complex

structure encountered in the real earth. Thus, we believe that there is a great need for a detailed description of the wave types represented by the ground motions.

In this study, we extend Hanks' study ( 1975 ) to examine the ground velocities and accelerations observed by the accelerograph array during the 1971 San Fernando earthquake. A display of the ground velocity profiles together with the topographic features and geologic structure ( Yerkes et al., 1965 ) will be presented and possible wave types and apparent phase velocities will be discussed.

Given the distribution of strong motion recordings of the San Fernando earthquake, it is possible to construct profiles along three azimuths. Figure 3-1 shows the station distribution and corresponding profiles. All profiles originate in the epicentral region. Profile I extends 65 km southward across the San Fernando and Los Angeles basins to a station on the Palos Verdes Peninsula. Profile II extends 95 km S40°E along the front of the San Gabriel mountains and then across the San Gabriel and Los Angeles basins. Profile III runs 90 km N40°W across the San Gabriel and Tehachapi mountains.

The San Fernando earthquake was also well recorded by strong motion instruments which are required in high-rise buildings. These buildings are clustered in three locations on the north side of the Los Angeles basin; the Miracle Mile area of Wilshire Boulevard ( local array 1 ), downtown Los Angeles ( local array 2 ), and Century City ( local array 3 ). Station locations for these dense local arrays are shown in Figure 3-2.

Time histories of ground velocity and acceleration are all taken directly from EERL, Caltech reports ( 1974 ). Ground motions are rotated into radial,

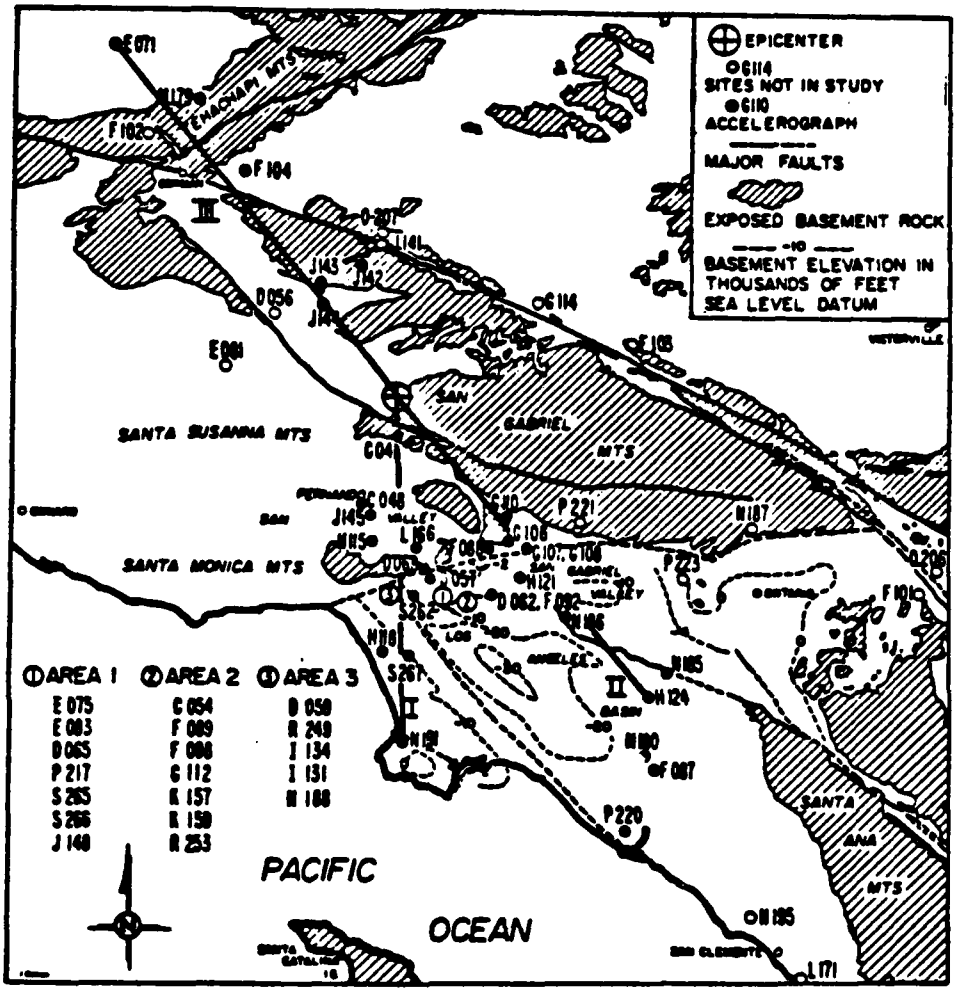


Figure 3-1 The long profiles, I, II and III, and site locations of accelerometer recordings of the 1971 San Fernando earthquake ( modified from Hanks, 1975 ).

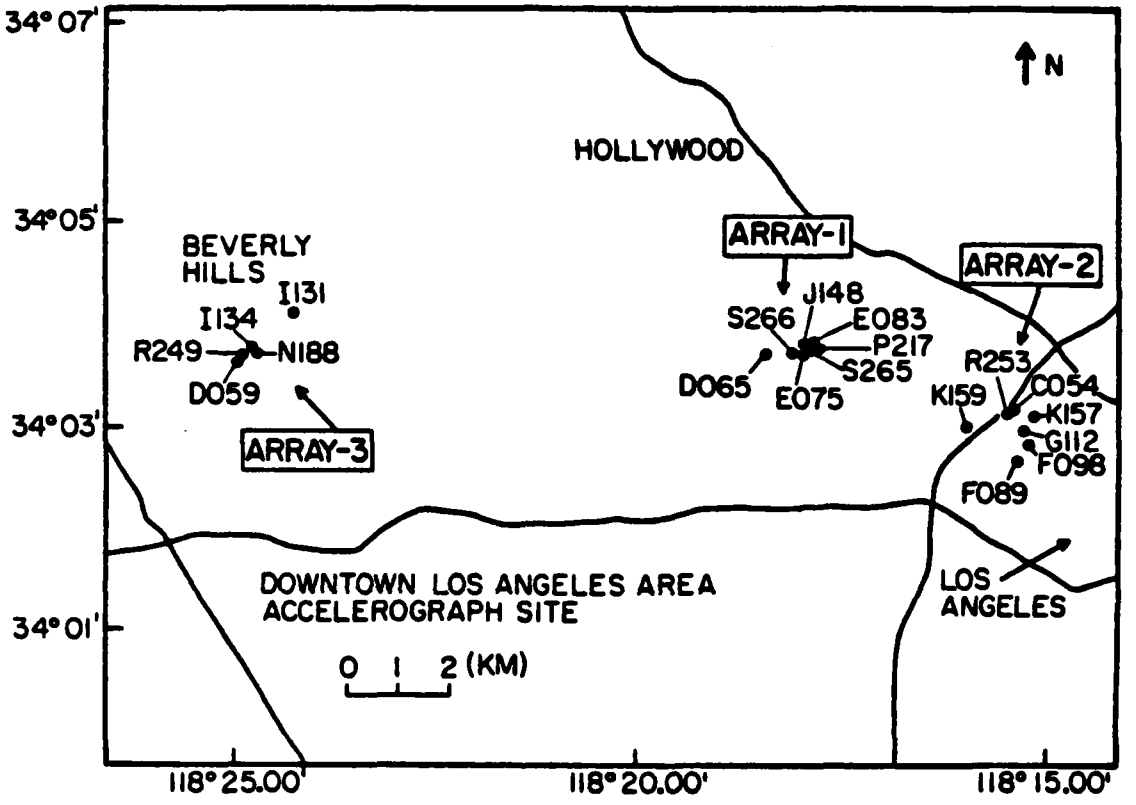


Figure 3-2 The site locations of 3 local arrays used in this study.

transverse, and vertical components and are then displayed as functions of time and distance from the epicenter as reported by Allen et al. ( 1973 ). Since absolute time is not available for any records, some assumptions need to be made to correlate phases from one station to another. We shifted records such that the apparent first shear-wave arrivals, which are named S! by Hanks ( 1975 ), are aligned vertically in the profile. S! minus trigger times are listed in Table 3-1 for all stations used in this study. Unfortunately, in some cases, the identification of S! is very difficult, and thus some of the more distant stations are probably not aligned on the first shear-wave arrival. Once the profiles are constructed, we find that the ground velocity waveforms are surprisingly coherent from station to staion, allowing us to estimate apparent phase velocities, to identify possible wave types, and qualitatively separate the source from the path effects. The features of each profile will be described in more detail as follows.

**Long Profiles**

**a. Profile I.** The velocity traces together with the corresponding free surface and basement surface topography profiles are displayed in Figure 3-3. Velocity traces begin with the S! arrivals. The two-fault system suggested by Heaton (1982) is also illustrated in the same Figure. H1 is the first hypocenter which ruptured along the Sierra Madre fault, and 4 seconds later, the second hypocenter H2 initiated on the San Fernando fault. According to Heaton's (1982) interpretation, the high peak velocity observed at station C041 (Pacoima Dam) is caused by rupture directivity along the Sierra Madre fault. Although the faulting process is rather complicated, the total source time duration is only about 7 seconds. We believe that the signal duration at Pacoima Dam (C041)

## Table 3-1 S! minus trigger times

| Station | Time(sec) | Station(#Fl.) | Time(sec) |
|---|---|---|---|
| Azimuth I | | Local Array-1 | |
| C041 | 3.0 | D065(11) | 0.0 |
| C048 | 1.6 | E075(11) | 1.3 |
| D057 | 1.1 | E083(7) | 0.8 |
| D068 | 0.0 | J148(17) | 5.6 |
| H115 | 4.0 | P217(12) | 0.8 |
| H118 | 0.0 | S265(31) | 5.6 |
| J145 | 1.6 | S266(21) | 5.6 |
| L166 | 1.3 | Local Array-2 | |
| N191 | 0.0 | C054(39) | 1.3 |
| S262 | 1.9 | F089(8) | 5.1 |
| S267 | 6.1 | F098(8) | 4.5 |
| Azimuth II | | G112(43) | 1.9 |
| G110 | 1.3 | K157(16) | 2.7 |
| G106 | 2.1 | K159(8) | 4.3 |
| G108 | 4.3 | R253(10) | 5.6 |
| H121 | 5.6 | Local Array-3 | |
| M180 | 0.0 | D059(19) | 0.0 |
| F087 | 0.0 | I131(10) | 5.6 |
| N186 | 0.0 | I134(15) | 6.1 |
| P220 | 0.0 | N188(16) | 5.6 |
| Azimuth III | | R249(27) | 5.1 |
| E071 | 0.0 | | |
| F102 | 0.0 | | |
| F104 | 0.0 | | |
| J142 | 5.0 | | |
| J143 | 0.0 | | |
| J144 | 0.0 | | |
| M179 | 0.0 | | |

# Building height in terms of floors.

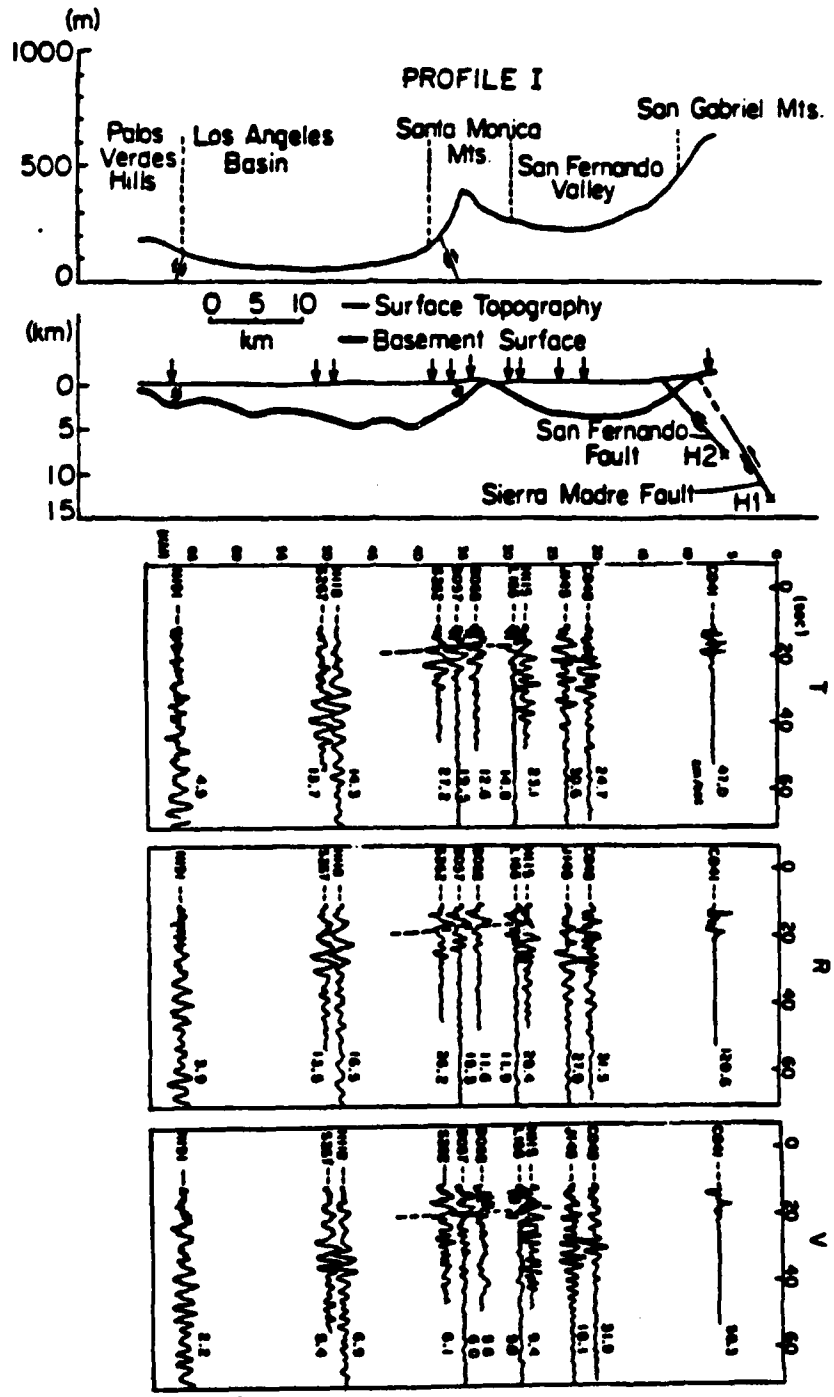


Figure 3-3 Transverse, radial and vertical components of ground velocity along profile I. The corresponding free surface and basement surface are shown on the top. Dashed lines crossing 30 km to 40 km indicate the possible phase arrivals of the surface waves.

represents the approximate duration of the source.

One of the most impressive features seen in Figure 3-3 is the correlation of ground motion waveform with the topography of the subsurface basins. There are three stations C048, J145 and H115 located within the San Fernando Valley. The waveforms recorded at these stations are poorly correlated and the signal durations are about 30 seconds. These durations are much longer than those seen at neighboring and more distant stations located near Santa Monica Mts., such as L166, D068 and D057. This contrast can easily be seen in Figure 3-3. Coherent waveforms begin to appear at station L136 and signal durations drop to only about 10 seconds. Furthermore, the amplitudes also drop quite drastically by about one-half after passing the San Fernando Valley stations. Amplitudes again increase at stations D057 and S262 when the waves reach the Los Angeles Basin. The waveforms are quite coherent in the beginning 6 seconds and there appears to be little moveout from the S! phase. The dashed lines passing stations L166, D068, D057 and S262 indicate the possible arrival of surface waves, which are characterized by gradual moveout from the S phases. They also appear dispersive in nature, this was also suggested by Hanks ( 1975 ) from his study of particle trajectories. It seems that, at epicentral distances of near 30 km, body waves dominate the waveforms at the bedrock sites, and the surface waves start to develop rapidly from there. For epicentral ranges beyond 40 km, surface waves start to dominate the wavetrain. At ranges of 50 km and beyond, it is hard to identify the body waves. Most of the signals appear to be surface waves with visibly dispersive character. The apparent moveout velocity of the surface wave phase from S! phase is estimated to be 5.7 km/sec. If we assume that the phase velocity corresponding to the S! phase is 3.5 km/sec, then the

phase velocity of these surface waves is about 2.2 km/sec.

It is useful to contrast the nature of wave propagation for waves observed in the San Fernando valley and the Los Angeles basin. Peak ground velocities observed in both basins are high with respect to sites in the Santa Monica mountains. Although long-period surface waves are clearly visible in both basins, the duration of these surface waves is up to 20 seconds longer in the San Fernando valley, the basin which is closer to the earthquake source. The earthquake ruptured into the northern part of the San Fernando valley which is a closed sedimentary basin. Thus it is likely that the long signal durations are caused by surface waves which are trapped within the valley, thereby causing severe ringing. The short signal durations seen at adjacent stations indicates that these reverberating waves which developed in the San Fernando valley did not propagate away from the valley. The interpretation from the numerical simulation result will be presented later.

In Figure 3-4, we show the radial components of the ground acceleration for stations located along profile I. Traces begin at their trigger time and are aligned vertically with the S! phase. Although there is considerable variation in the observed waveforms from station to station, the duration of the high-frequency motions is a fairly constant 10 seconds. Furthermore, strong phases can be seen on many records at about 4 seconds and 8 seconds after the initial S arrivals. We speculate that the overall duration and timing of arrivals seen on the relatively high-frequency acceleration time history is directly related to the details of the faulting process. It is suggested that the basin geometry has less effect on these higher frequency waves.

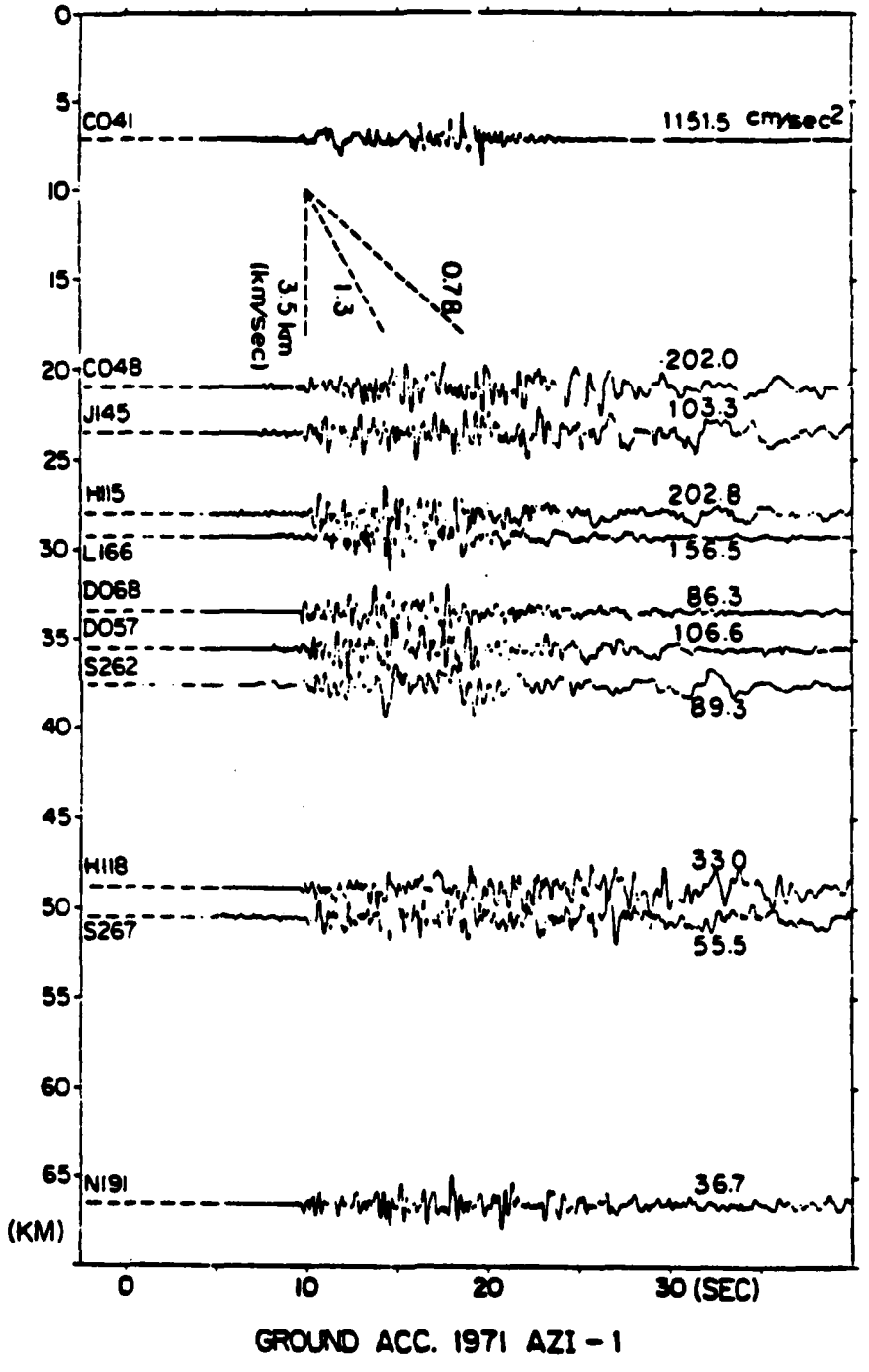


Figure 3-4 The radial component of ground acceleration along profile I.

**b. Profile II.** Profile II is roughly along the southwest border of the San Gabriel mountains and part of the Los Angeles basin. The velocity traces (beginning at S!) together with the path profile are shown in Figure 3-5. Somewhat different features are observed along this profile. The signal duration of what appear to be mainly the S! phase is about 8 seconds at station G110. Surface waves develop gradually with distance from there. The amplitudes along this path are, on average, lower than those in Profile I. Perhaps part of the reason for this is the lack of thick sediments along profile II from about 30 km to 50 km. Well dispersed surface waves can hardly be identified at this portion of the profile. Instead, the S! phase, which is characterized by zero moveout can still easily be recognized. Even at station N186, which has an epicentral distance of 52 km, the high-frequency S! phase can still be identified, this suggests that the relatively thin sediments along profile II prohibit the rapid development of the surface waves seen in profile I. However, there may still be a strong fundamental Rayleigh wave which is hard to distinguish from the S wave ( see Heaton and Helmberger, 1979 ). The dashed lines crossing station G110 to station N186 indicate the possible surface wave phases. If we assume a horizontal phase velocity of 3.5 km/sec for the S! phase, then the phase velocity corresponding to the dashed line is approximately 2.7 km/sec.

In Figure 3-6, we show the radial components of the ground acceleration for stations located along Profile II. Peak amplitudes and the duration of high-frequency shaking are remarkably similar to that seen along Profile I. However, the strong phases seen at 4 and 8 seconds in S wavetrain on Profile I are not as evident in Profile II. Instead, the strongest phase seen along Profile II appears to be about 6 seconds after the beginning of the S wavetrain.

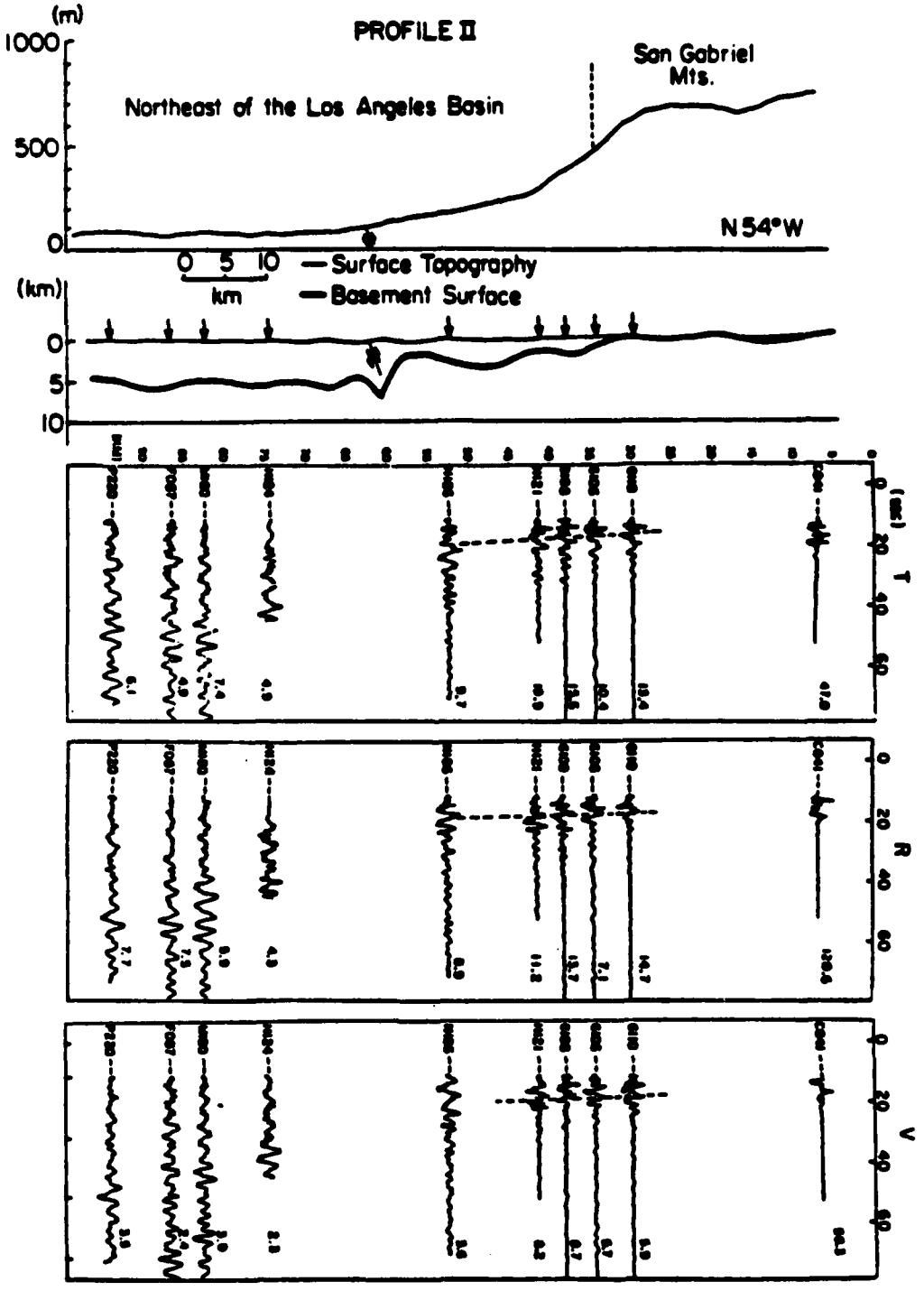


Figure 3-5 Transverse, radial and vertical components of ground velocity along profile II. The corresponding topography and the basement surface are shown on the top. Dashed lines indicate the possible phase arrivals of surface waves.

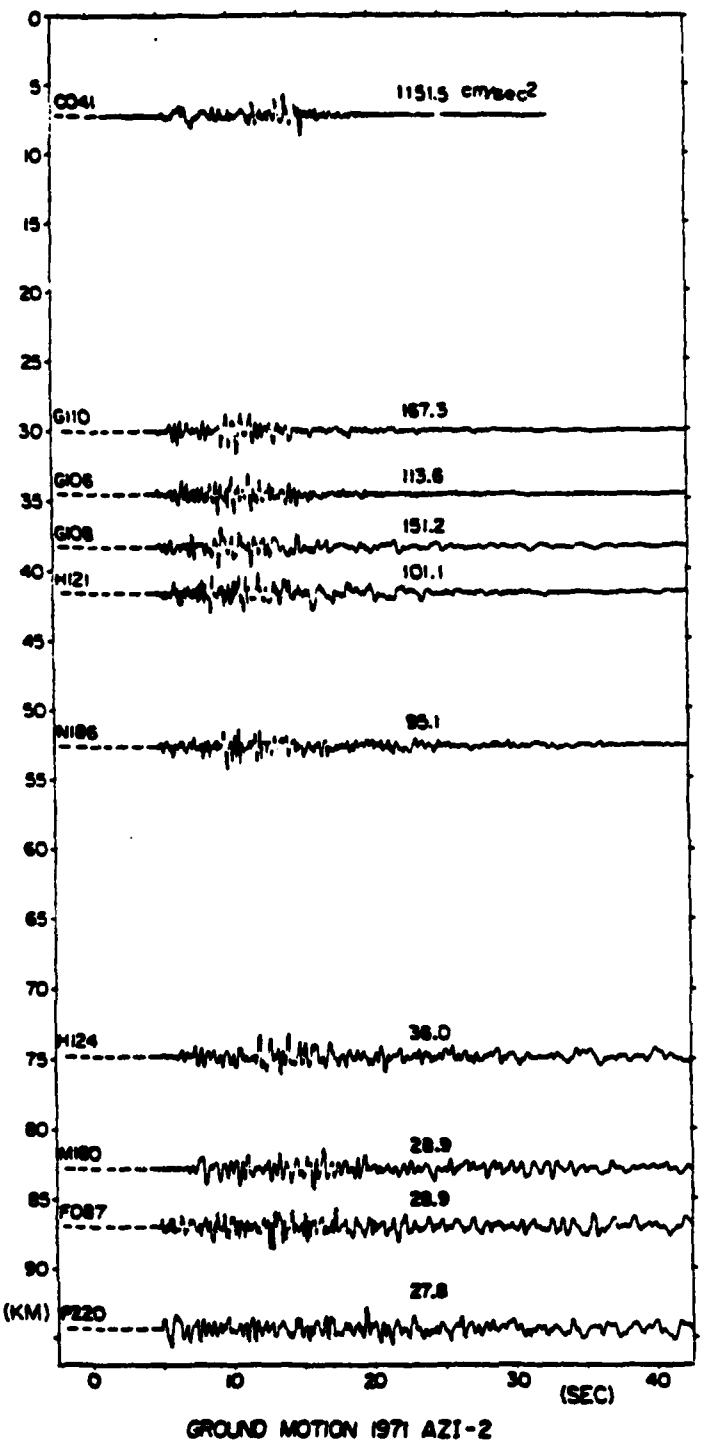


Figure 3-6 The radial component of ground acceleration along profile II.

**c. Profile III.** Profile III runs N40° W across mostly mountainous terrain and ground velocity traces along this profile are shown in Figure 3-7. Ground velocities are strikingly different along this profile from the other two profiles, which cross deep sedimentary basins. The duration and amplitude of the ground velocity seem to be considerably less on this northern profile. Heaton and Helmberger ( 1979 ) shows that displacements observed at station J142 can be reasonably modeled with a simple half-space structure. This is obviously not the case for many of the stations located along profiles I and II.

Radial ground accelerations observed along Profile III are shown in Figure 3-8. Ground accelerations appear to be shorter-period and of shorter duration than those observed along the other two profiles. Furthermore, it is difficult to identify any coherent phases.

In Figure 3-9, we compare peak radial velocities amplitudes along the three profiles. It seems clear that peak velocities are larger on stations to the south, except for those stations on or adjacent to the Santa Monica or San Gabriel mountains. It appears likely that the deep sedimentary basins are the principal reason for this amplitude variation.

In Figure 3-10, we compare peak radial acceleration amplitudes along the profiles. Peak accelerations are surprisingly similar for these three profiles. This conclusion was previously reported by Trifunic ( 1976 ). Using data mainly from the San Fernando earthquake, he concluded that peak ground motions were greater on 'soft' sites than on 'hard' sites, with the effect being considerable at long periods and almost negligible at high-frequencies.

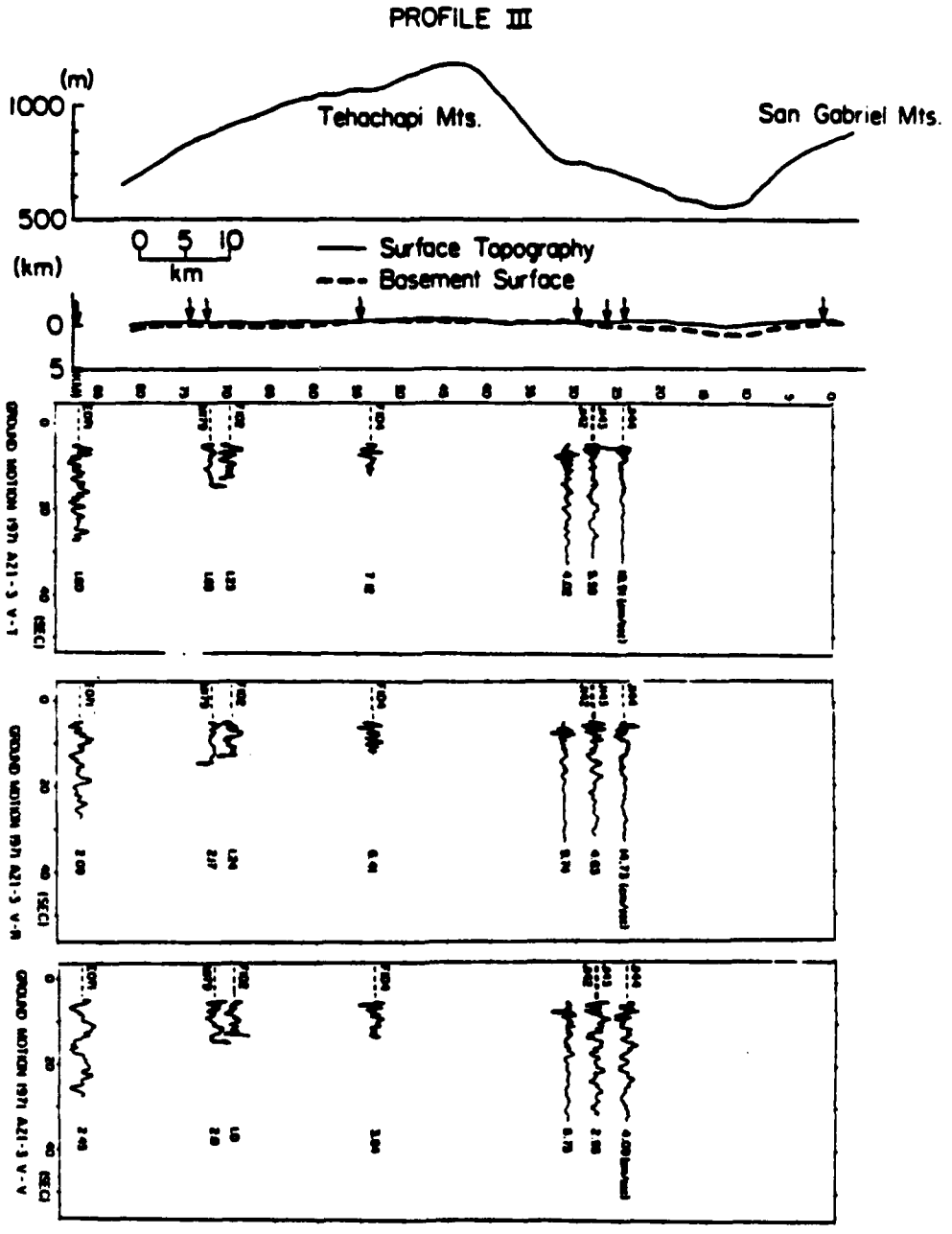


Figure 3-7 Transverse, radial and vertical components of ground velocity along profile III. The corresponding topography and the basement surface are shown on the top.

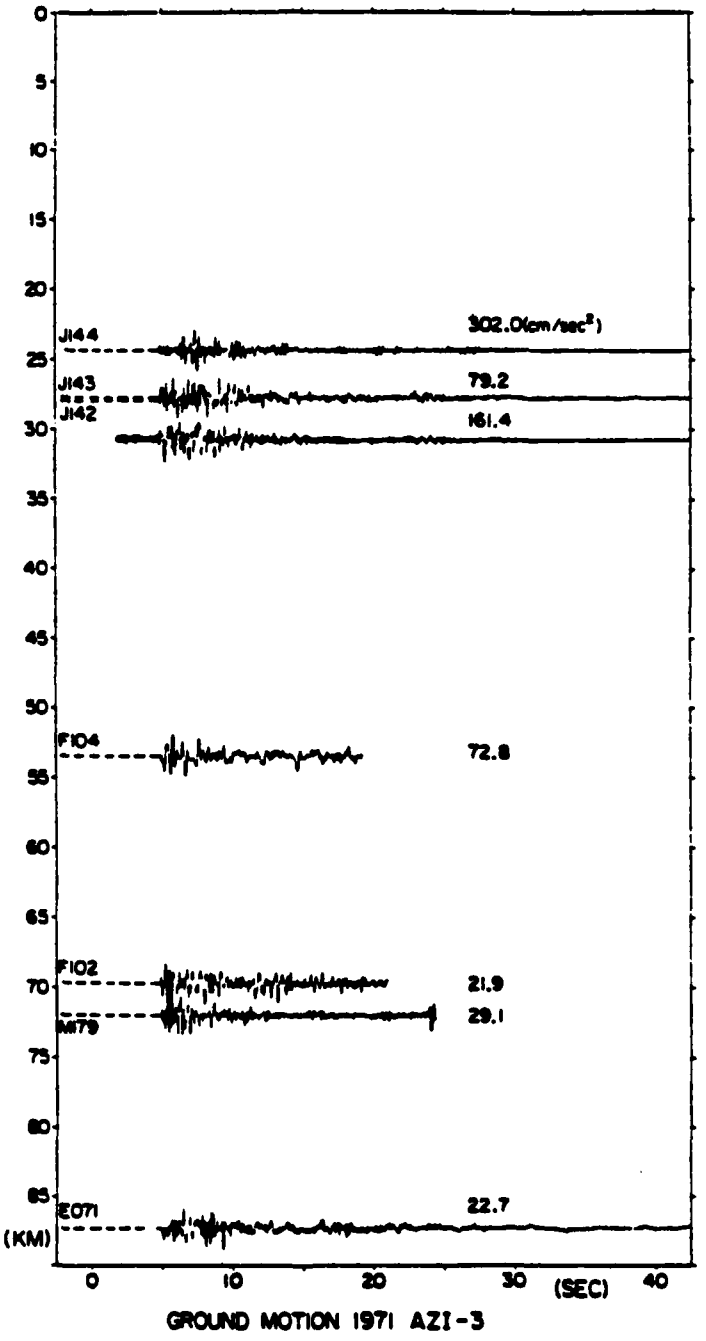


Figure 3-8 The radial component of ground acceleration along profile III.

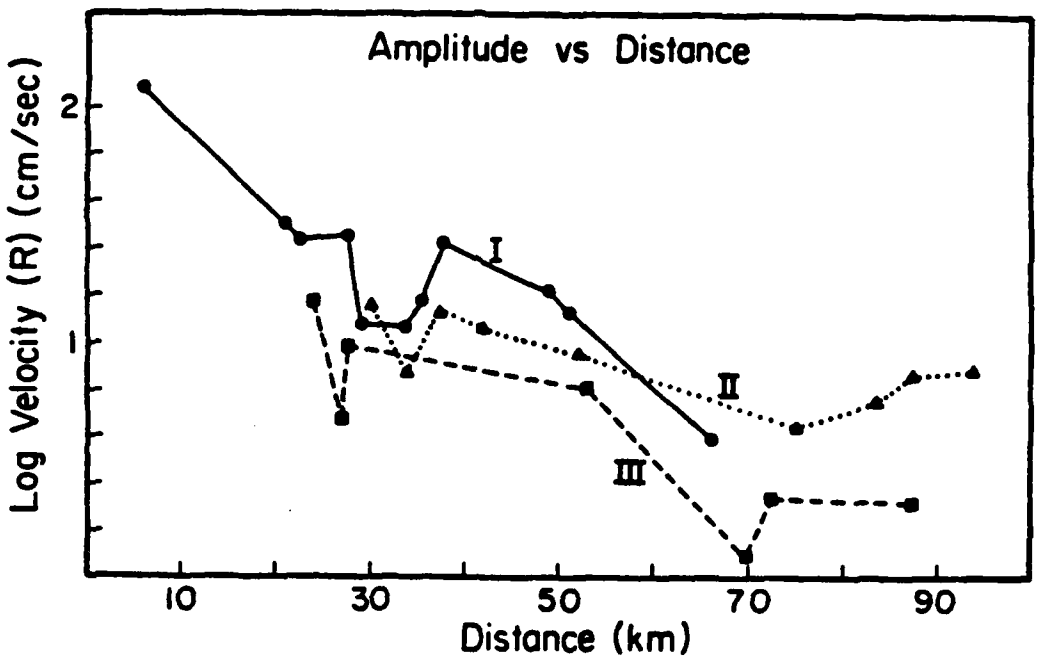


**Figure 3-9** Peak radial velocities vs. epicentral distance for the three long profiles.

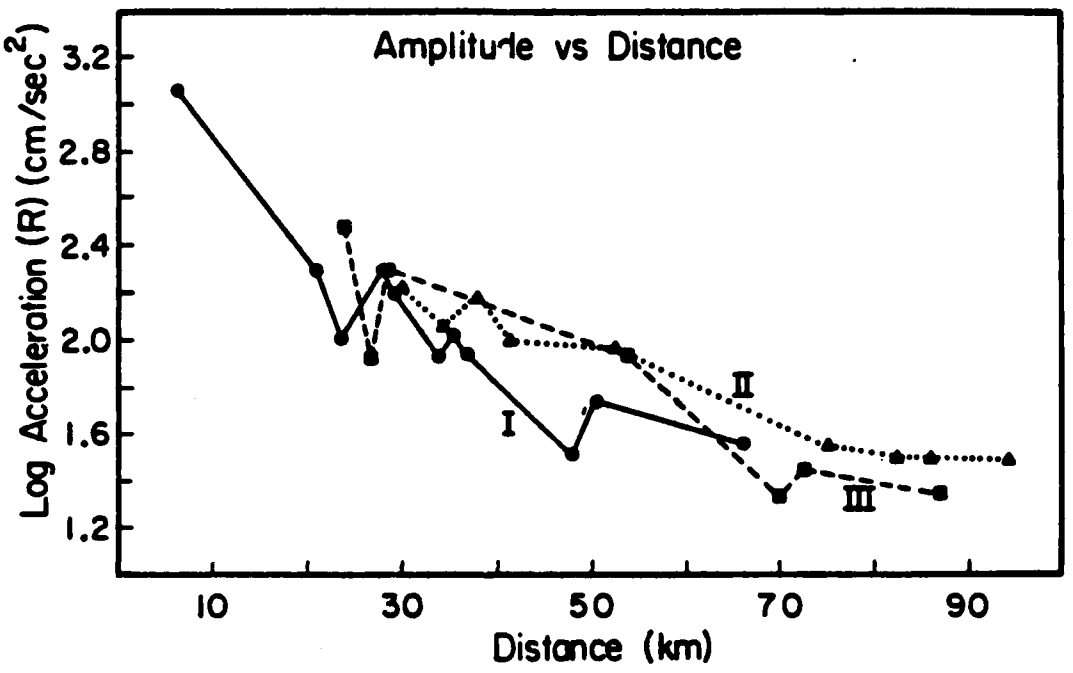


Figure 3-10 Peak radial accelerations vs. epicentral distance for three long profiles, I, II, and III.

**Local Arrays**

In Figure 3-11, 3-12 and 3-13, we show three components of ground velocity as functions of time and epicentral distance for local arrays 1, 2 and 3, respectively. Since stations in these arrays are not generally aligned along a radial line from the epicenter, the distances shown in Figure 3-11 through 3-13 may not be indicative of the true inter-station spacing.

The most obvious feature of the ground velocity is the remarkable degree of coherence across each array. Since the velocity waveforms are dominated by waves with frequencies of less than 5 Hz, we expect that most of the motion has horizontal wavelengths of greater than 0.5 km. Thus, there is good reason to expect the ground velocity to be coherent over these small arrays. However, there are several other implications of this coherence. First, the record processing must introduce very little noise into the velocity traces. This is especially impressive when one considers that the horizontal components require component rotations before they can be compared. Second, the effect of building interaction is apparently minimal on velocity waveforms. The average standard derivation of peak velocity within each array is about 12%. Furthermore, it is difficult to see the systematic dependence of peak velocity with building height (see Table 3-1) within each array that is suggested by Boore et al. ( 1980 ).

We show the radial component of ground acceleration for local array 1 in Figure 3-14. Although less coherent than the velocities, accelerations still show strong coherence along the profile. Prominent phases can be seen at 2, 4, and 8 seconds after the initial S! phase. It is difficult to see moveout of any phase for these local arrays. This is not surprising since a variation in phase velocity between 4 and 2 km/sec yields a moveout of only .25 sec/km. Such small time

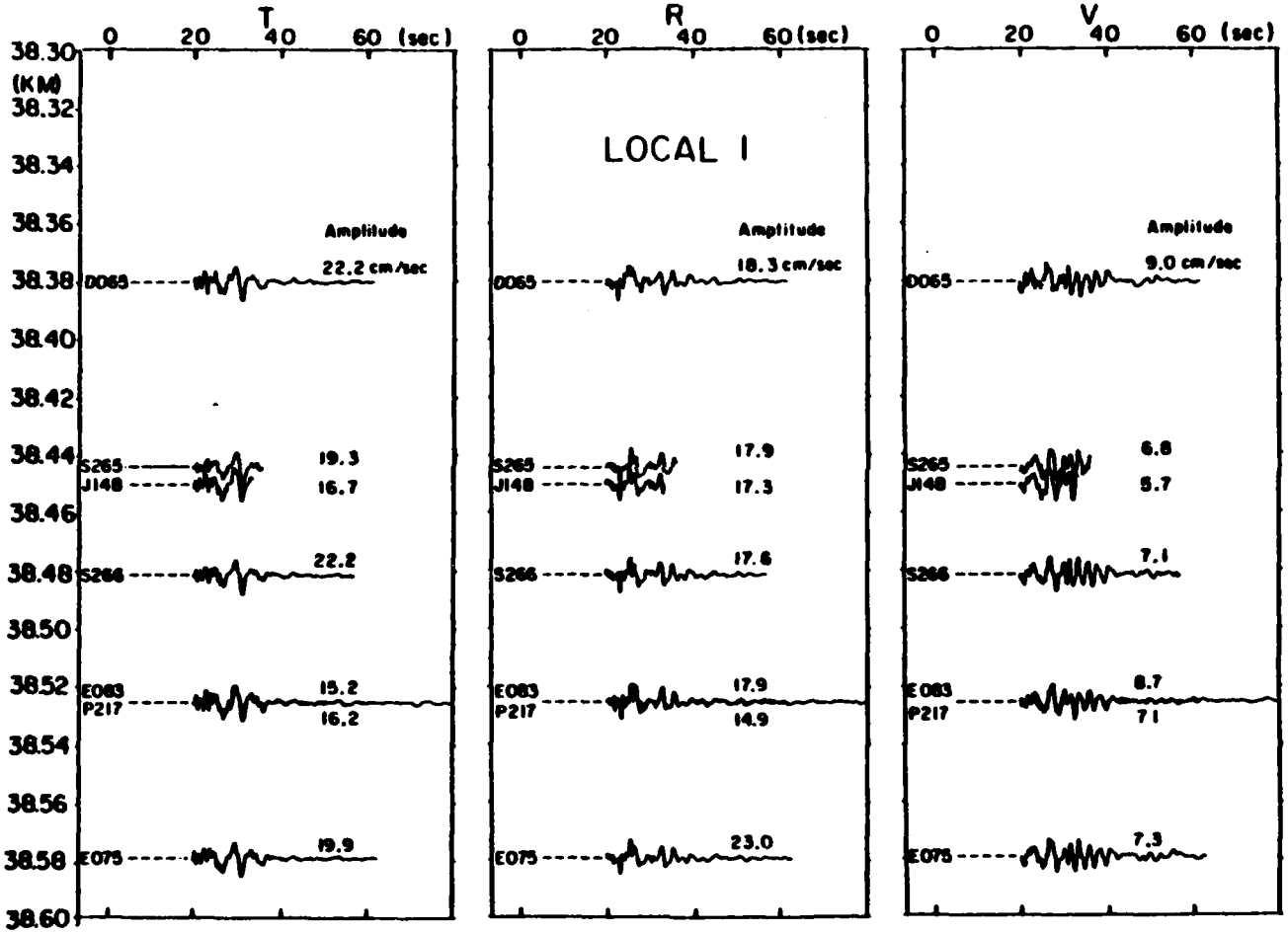


Figure 3-11 Transverse, radial and vertical components of ground velocity in local array-1.

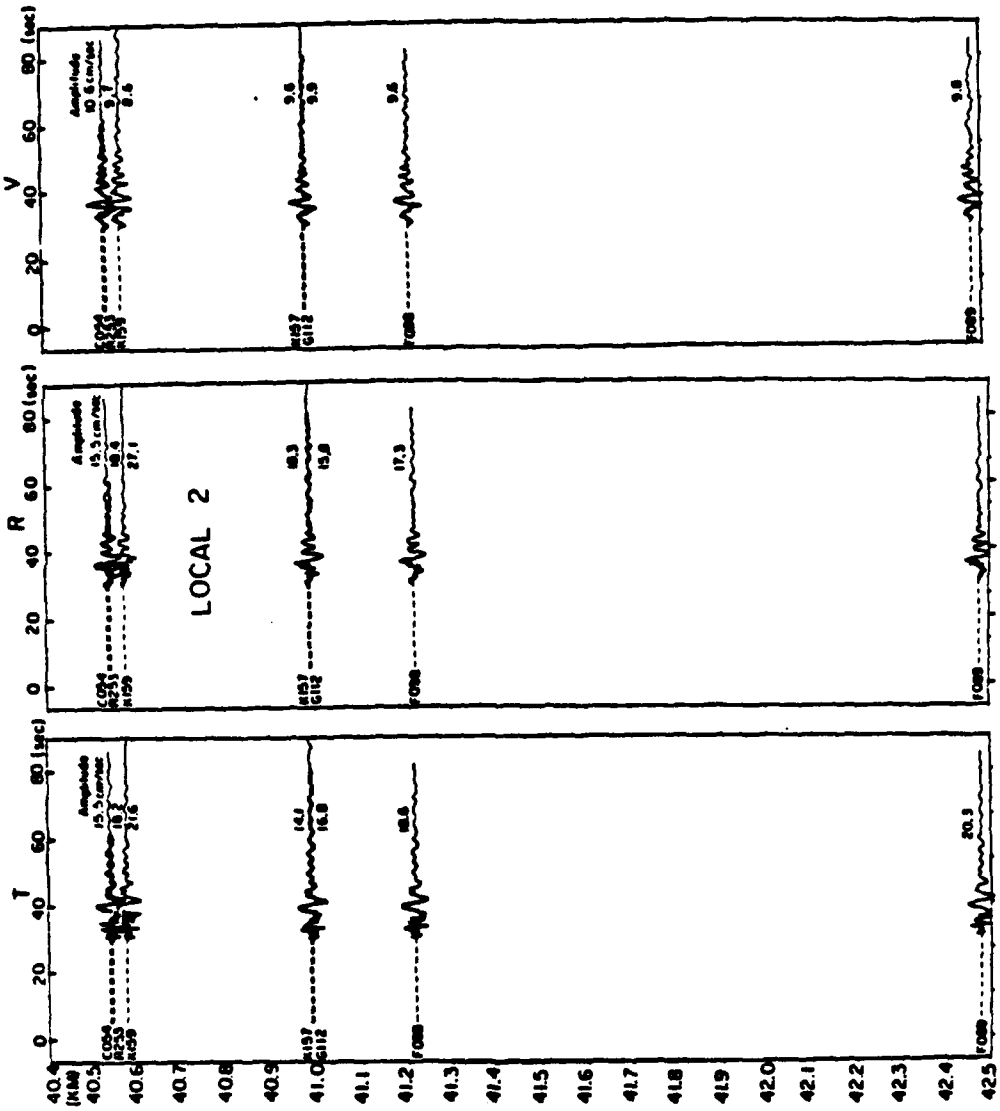


Figure 3-12 Transverse, radial and vertical components of ground velocity in local array-2.

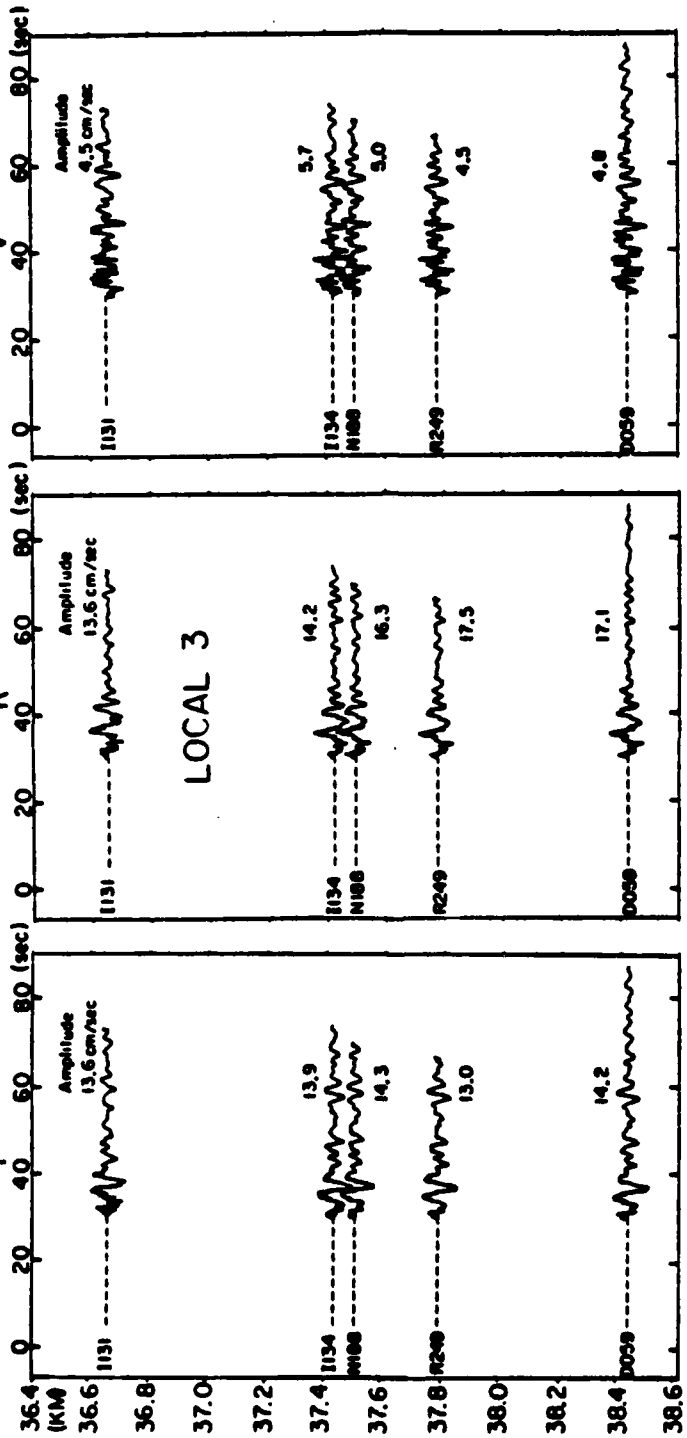


Figure 3-13 Transverse, radial and vertical components of ground velocity in local array-3.

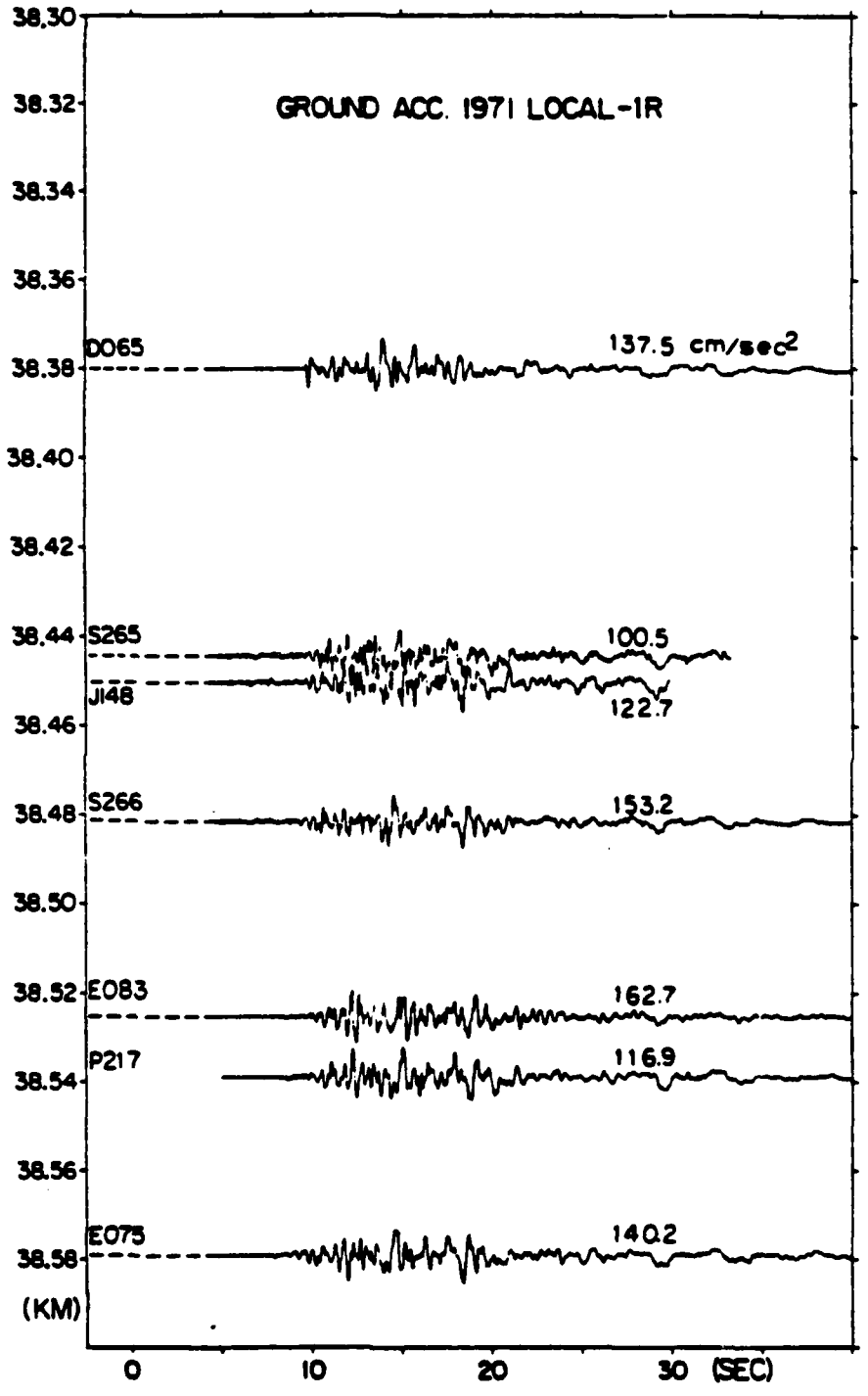


Figure 3-14 The radial component of ground acceleration in local array-1.

shifts could only be detected through very careful analysis.

**Simulation by Finite Difference Method**

The strong correlation of observed ground motions with geological structure profiles encourages our further investigation of these irregular structure effects. We use the acoustical 2D finite difference method ( Brown and Clayton, 1983) to generate synthetic seismograms along both profile I and profile II. The main emphasis here will be on phenomena which occur on waves propagating through these irregular structures from different source depths. We investigate amplitude amplification, signal duration and wave type development.

According to Heaton's ( 1982 ) double event solution for the 1971 San Fernando earthquake, there are mainly two areas in which the dislocation is concentrated. One area is near the first hypocenter at a depth of about 13 km and has a maximum dislocation of about 2.5 meters. Another is very near the surface ( at depth of about 1 km ) along the San Fernando fault with a maximum dislocation of about 3.5 meters, as illustrated in Figure 3-15. In order to study the effect of sources at different depths, we calculated the structure response along each profile for three source depths, namely 1 km , 7km and 13 km. The difference method is applied to the 2D acoustical wave equation

$$\frac{\partial^2 P(x,z)}{\partial t^2} = v^2(x,z)\cdot\nabla^2 P(x,z)$$

, where $x,z$ are the 2D coordinates and $v(x,z)$ is the medium velocity. The normal stress or the pressure $P(x,z)$ is continuous along all boundaries and vanishes on the free surface. The details are described in a paper by Brown and

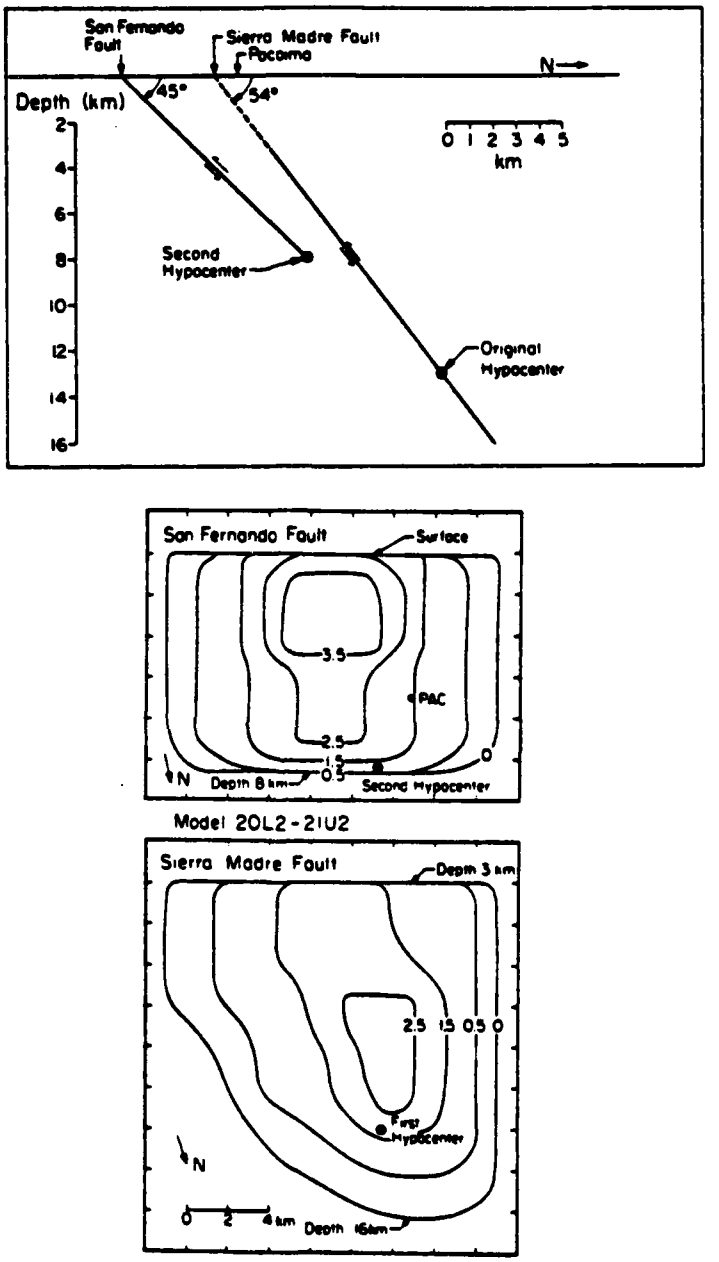


**Figure 3-15 The dislocation distribution along the two faults in 1971 San Fernando earthquake determined by the waveform modeling of Heaton ( after Heaton, 1982 ).**

Clayton ( 1983 ). We used a 0.2 km grid size for both horizontal and vertical ranges, this corresponds to about 10 samples per wavelength at a period of 1 second. Since the maximum velocity in our model is 3.5 km/sec, we chose the difference time step $dt$ to be 0.03 seconds to satisfy the stability criteria,

$$dt < \frac{dh}{\sqrt{2} \cdot v_{max.}}$$

where $dh$ is the grid size. In this way we constrain the time step to be small enough that disturbances do not propagate faster than the maximum velocity within a grid.

**a. Irregular Structure along Profile I** We approximate earth structure along our profiles as a simple low-velocity ( 2.1 km/sec ) basin embedded within a high-velocity ( 3.5 km/sec ) bedrock half-space, as illustrated in the left of Figure 3-16(a). The source is introduced as an initial condition whereby wave motions in the source region are specified to be the derivative of a Gaussian function. The details can be found in Brown and Clayton ( 1983 ). All the profiles are computed assuming a 400x300 grid, which corresponds to dimensions of $80km \times 60km$. Synthetic seismograms computed along profiles 50 km long are shown in Figures 3-16(a), 3-16(b) and 3-16(c) for source depths of 1 km ( S3 ), 7 km ( S2 ) and 13 km ( S1 ), respectively. The total signal duration is 45-second for all the synthetic traces presented in this Chapter. Full scale amplitude is 0.07 for all the profile traces. Thus, waveform amplitudes are comparable for different sources.

Although the synthetics are computed assuming a 2D acoustic line source, the resulting synthetics show good resemblance to the observed ground

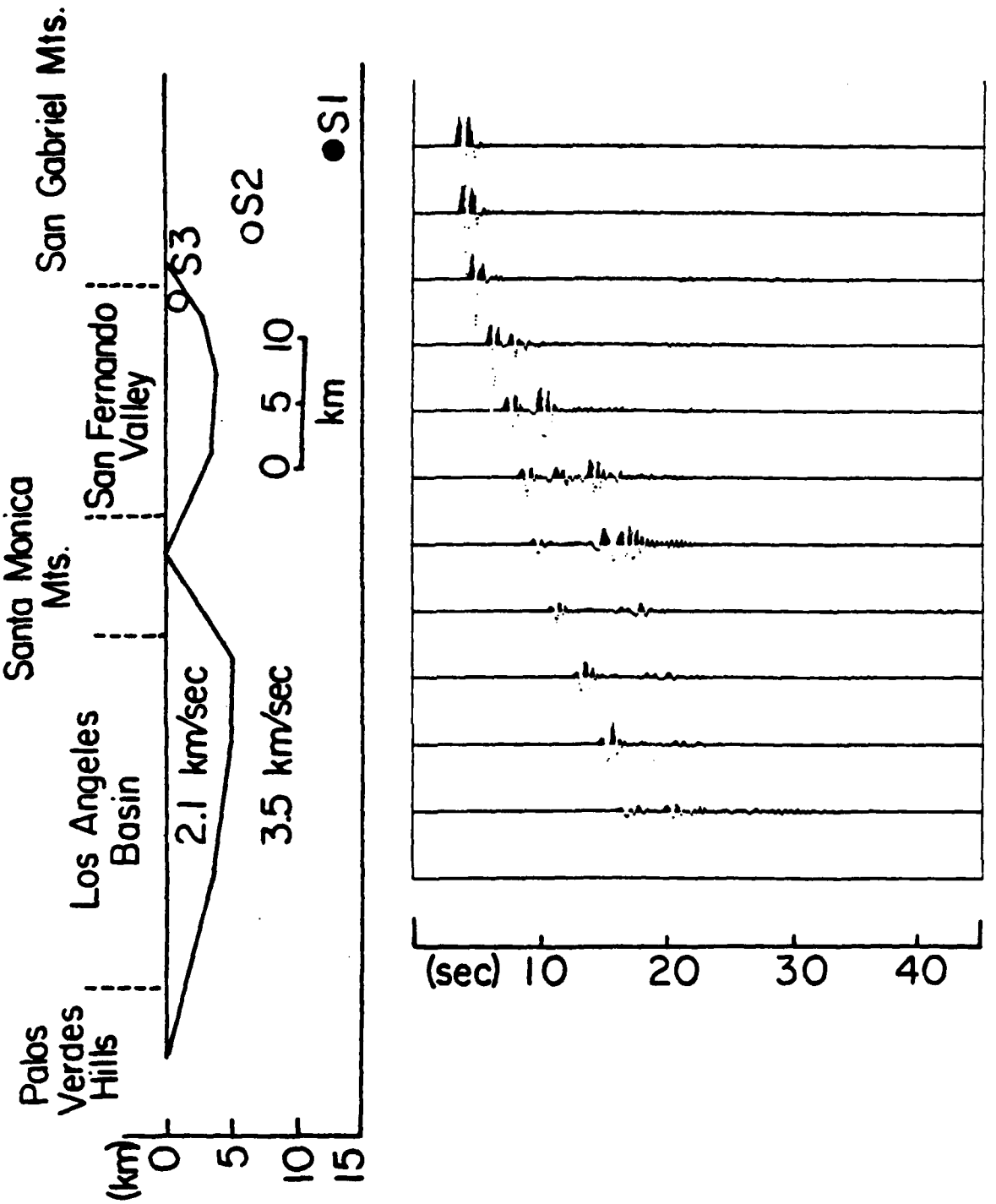


Figure 3-16(a) Synthetic seismograms along the profile I from a source at a depth of 13 km. The full scale amplitude is 0.07 for all the profile traces.

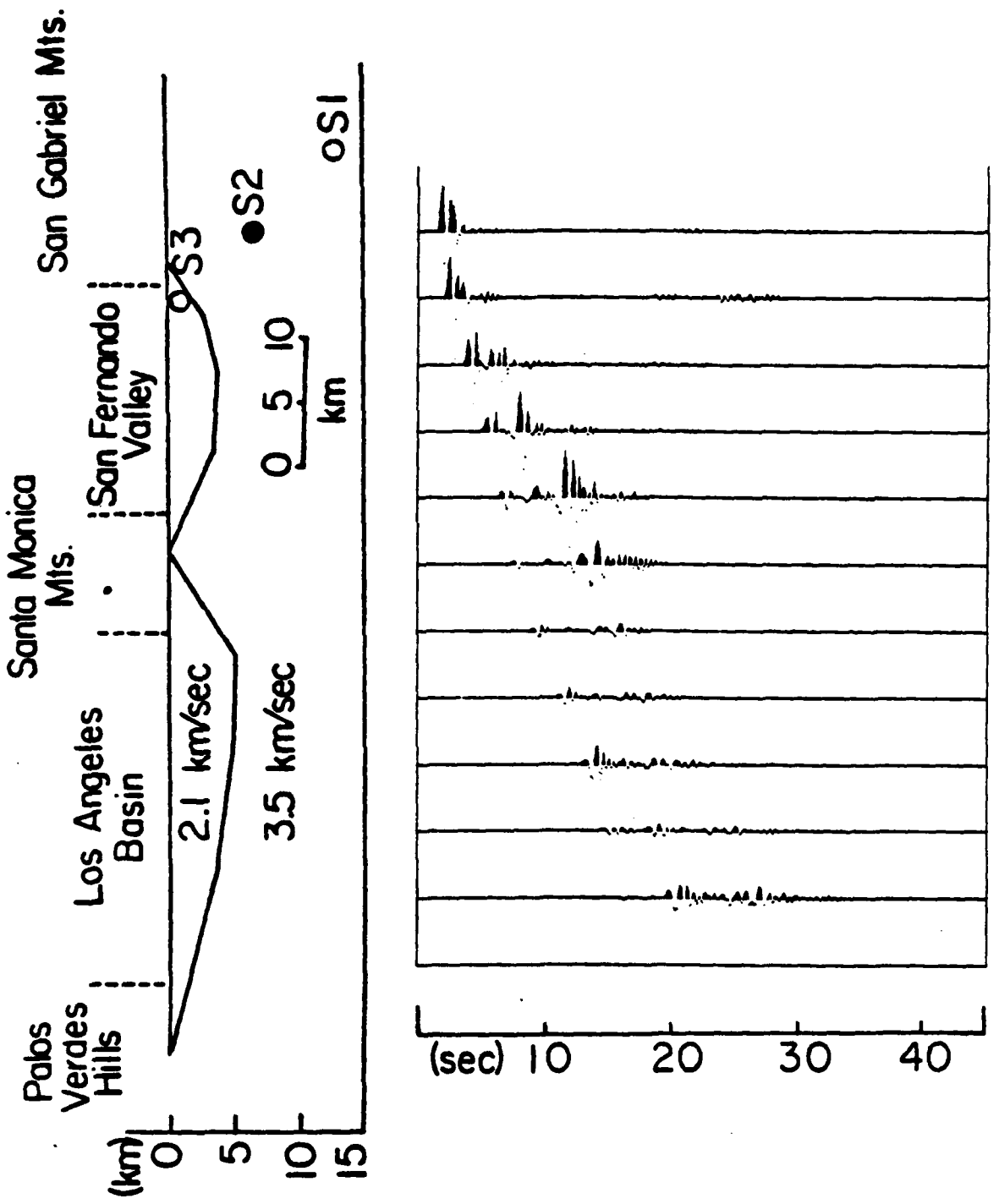


Figure 3-16(b) Synthetic seismograms along profile I from a source at a depth of 7 km.

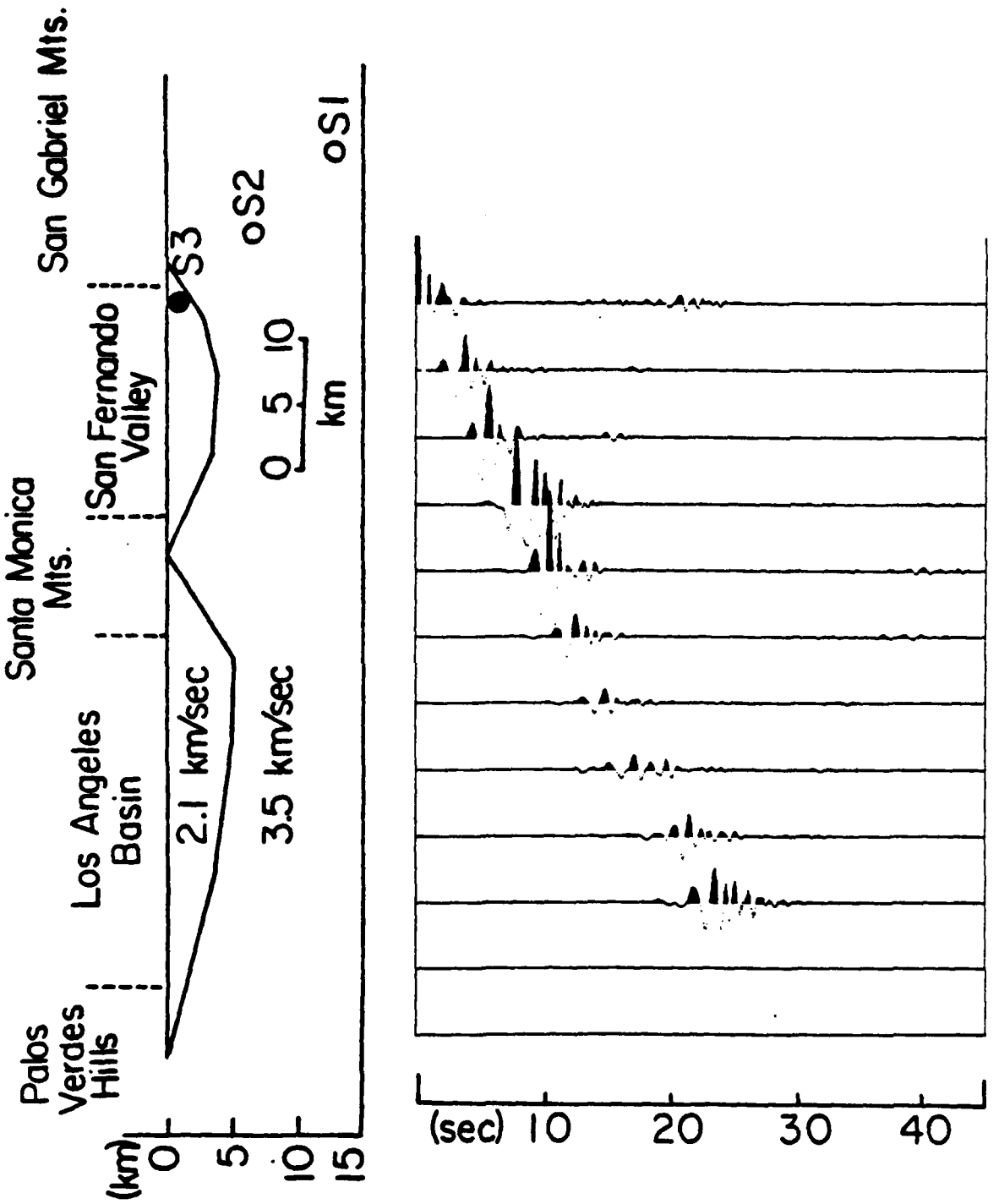


Figure 3-16(c) Synthetic seismograms along profile I from a source at a depth of 1 km.

velocities along profile I. In our model, the San Fernando Basin is an obstacle, creating a shadow for those receiver sites on the Santa Monica Mountains. The strong amplification in the San Fernando Basin can be seen very well for all three source depths. Strong energy focusing is seen near the edge of the basin. This phenomenon is discussed in more detail in Appendix II and is illustrated for a simpler geometry in Figures II-5, II-6 and II-7.

Little energy from the shallow source transmits into the ridge of basement (Santa Monica Mountains), which separates the two low-velocity basins. However, for deeper source ( say at 13 km ) direct arrivals actually become stronger in the ridge of basement since waves can reach this region from below the basin.

Entering the Los Angeles Basin, we see that surface waves become the dominant arrivals. Wave development here is similar to examples of down-dip wave propagation discussed in Appendix II ( see Figures II-1, II-2, and II-3 ). For the deeper sources, energy reaches the Los Angeles Basin without strong effects from the San Fernando basin. This can be recognized by comparing between the profiles in Figure 3-16(a) and Figure II-3. However, in this range, the interpretation of wave propagating through the ridge from the shallow source is not straightforward. We demonstrate this by comparing the synthetics along two different ridge structures. In Figure 3-17(a), the San Fernando basin is simulated by a simple soft layer with an up-dip thinning edge. The synthetic seismograms suggest that little energy propagates through the basin and into the half-space region beyond. However, when a second basin is added to form a ridge as illustrated in Figure 3-17(b), then surface waves gradually develop in the second basin after passing the ridge area. Thus, the energy leaking through the up-dip edge of the San Fernando basin is trapped again by the down-dip slope in the Los

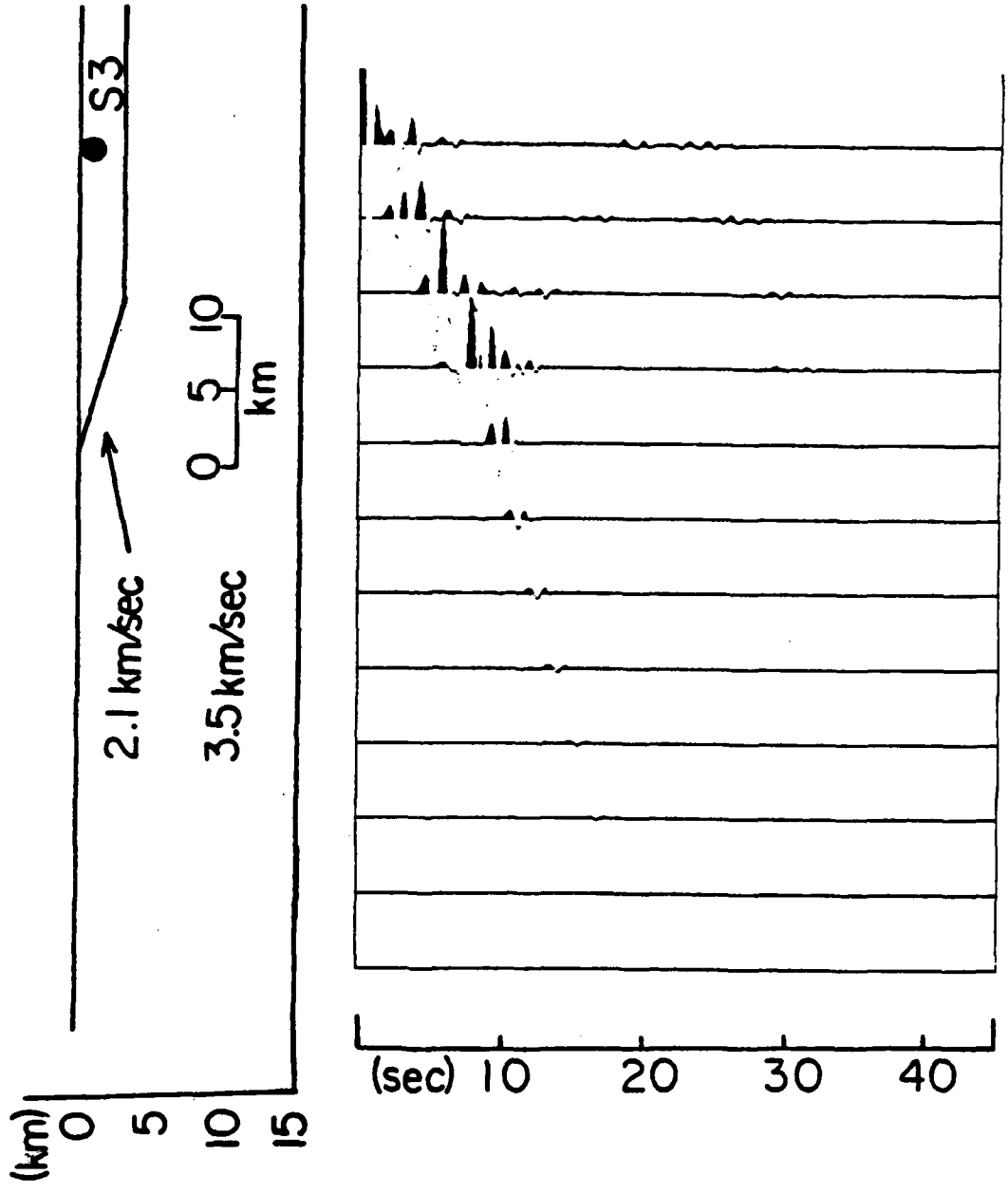


Figure 3-17(a) Ridge structure simulation; up-dip edge of the basin. This illustration shows that little energy can pass the up-dip basin edge and reach the surface receivers. Energy that leaks through the slope propagates mainly toward the half-space.

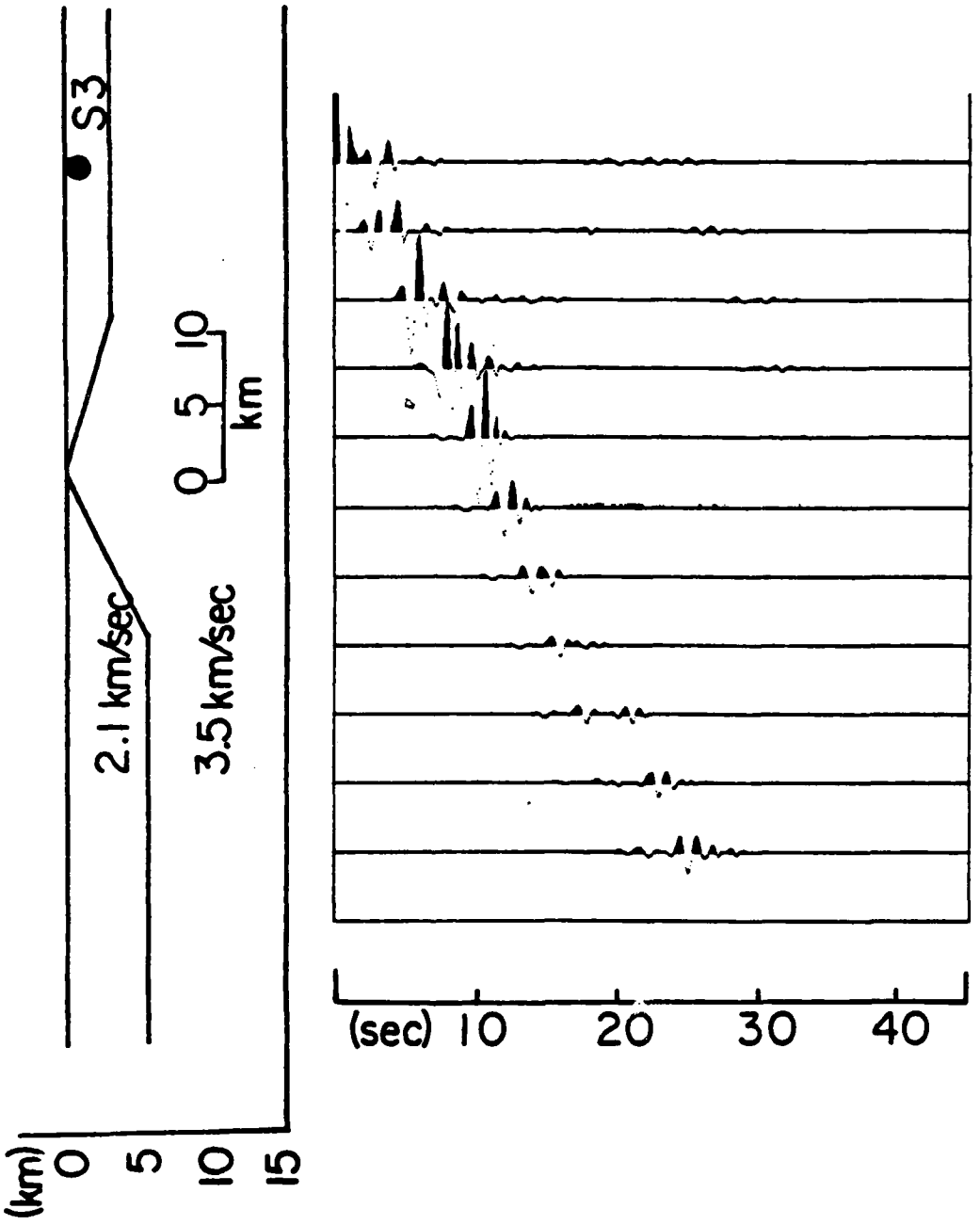


Figure 3-17(b) Ridge structure simulation; formed by both up-dip and down-dip edges of the basins. This ridge is constructed based upon the slopes seen from the San Fernando and Los Angeles basins. After passing the ridge, surface waves are gradually developed from energy trapped by the down-dip edge from Los Angeles basin.

Angeles basin to produce surface waves at further distances. The geometry of the ridge is an important for determining the amount of the energy which is trapped in the second basin.

Assuming Heaton's source model ( 1982 ), the rupture delay between source S1 ( at 13 km ) and S2 ( at 7 km ) is estimated to be about 4 seconds. Assuming that S1 and S3 ( at 1 km ) represent areas of the largest dislocations , we can roughly estimate the timing of arrivals and corresponding wave types seen along profile I. The time delay between S3 and S1 due to rupture is about 6 seconds and the corresponding travel time delay is about -4 seconds. Thus we concluded that the S! phases observed along profile I are mainly derived from S1 ( 13 km source ). The strong later arriving waves seen near the Santa Monica Mountains are surface waves from both S1 ( deep source ) and S3 ( shallow source ). For the three stations in the San Fernando Basin, C048, J145 and H115, the high amplitude waves seen in the velocity waveforms are combinations of surface waves from both deep and shallow sources and body waves from the shallow source. Thus, the reason that the S! phase maintains strong coherence along this structurally complex path is that S! is derived mainly from the deeper part of the rupture. The S! travel path from deeper sources is affected relatively little by the presence of local basins.

**b. Irregular Structure along Profile II** Ground motions observed along profile II show very different features from those observed along profile I. Again, we generate synthetic seismograms along the profile II for three source depths, namely 1 km ( source S3 ), 7km ( source S2 ), and 13 km ( source S1 ). The results are illustrated in Figures 3-18(a), 3-18(b) and 3-18(c), respectively. Since the wave path is more or less following the northeastern boundary of the

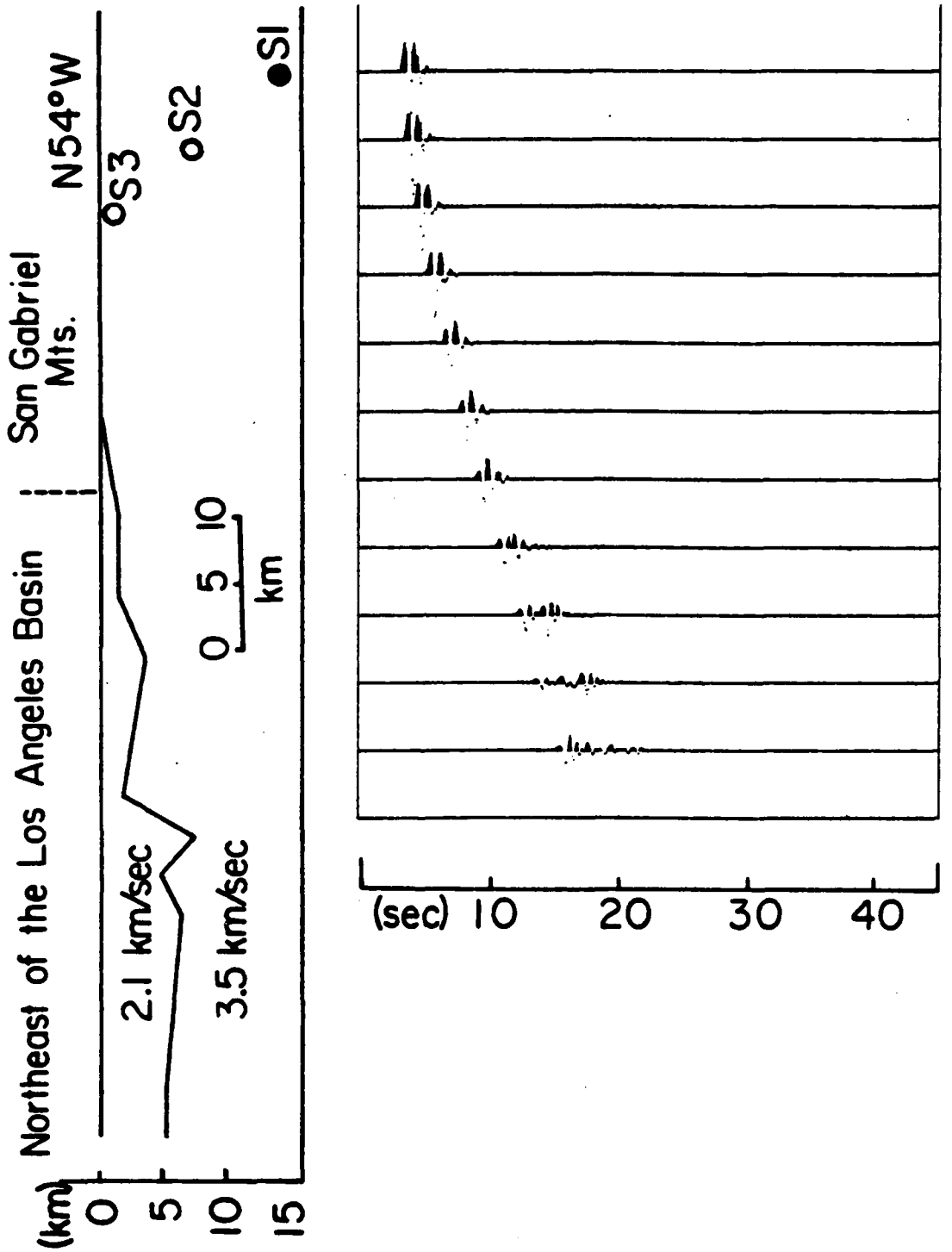


Figure 3-18(a) Synthetic seismograms along profile II from a source at a depth of 13 km.

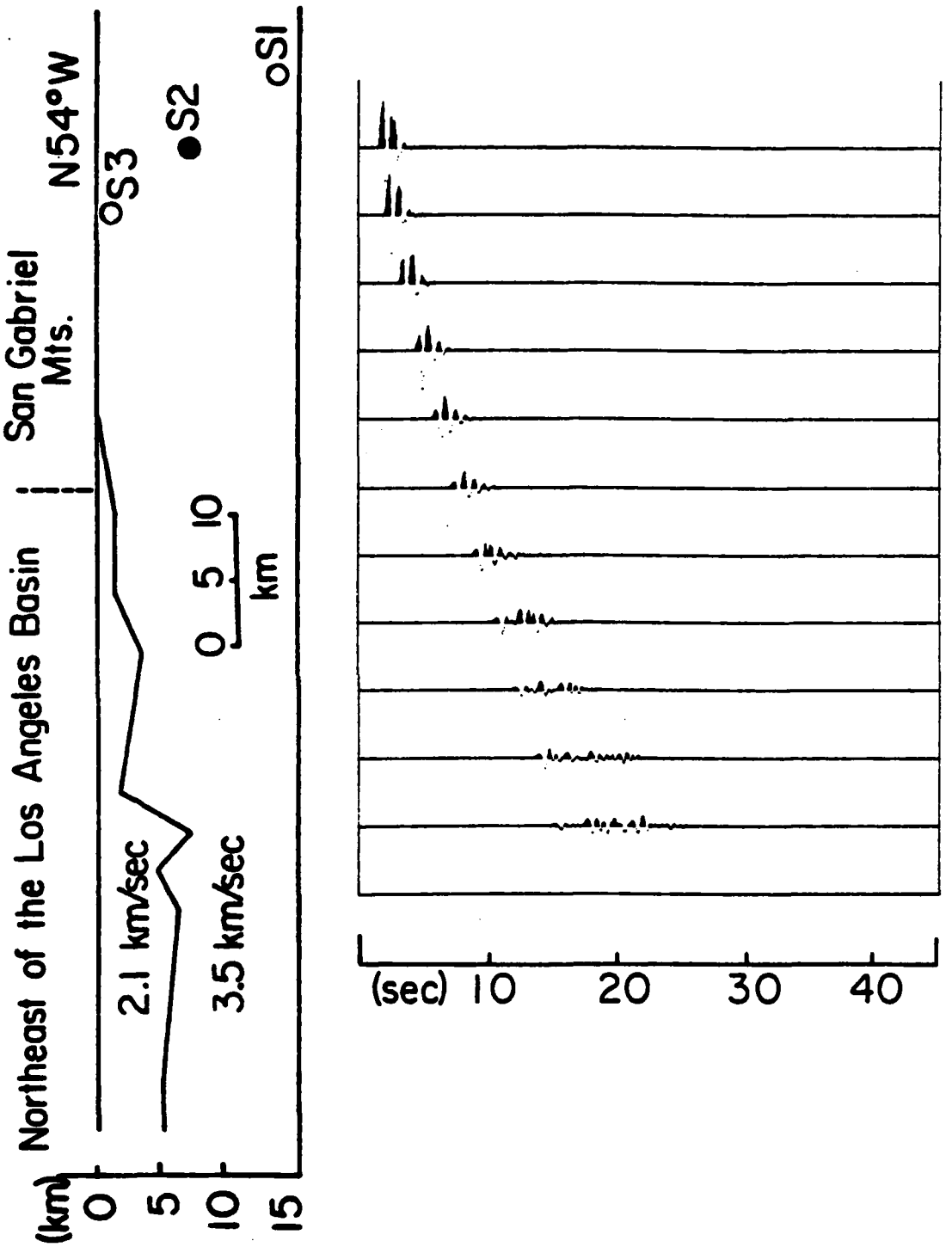


Figure 3-18(b) Synthetic seismograms along profile II from a source at a depth of 7 km.

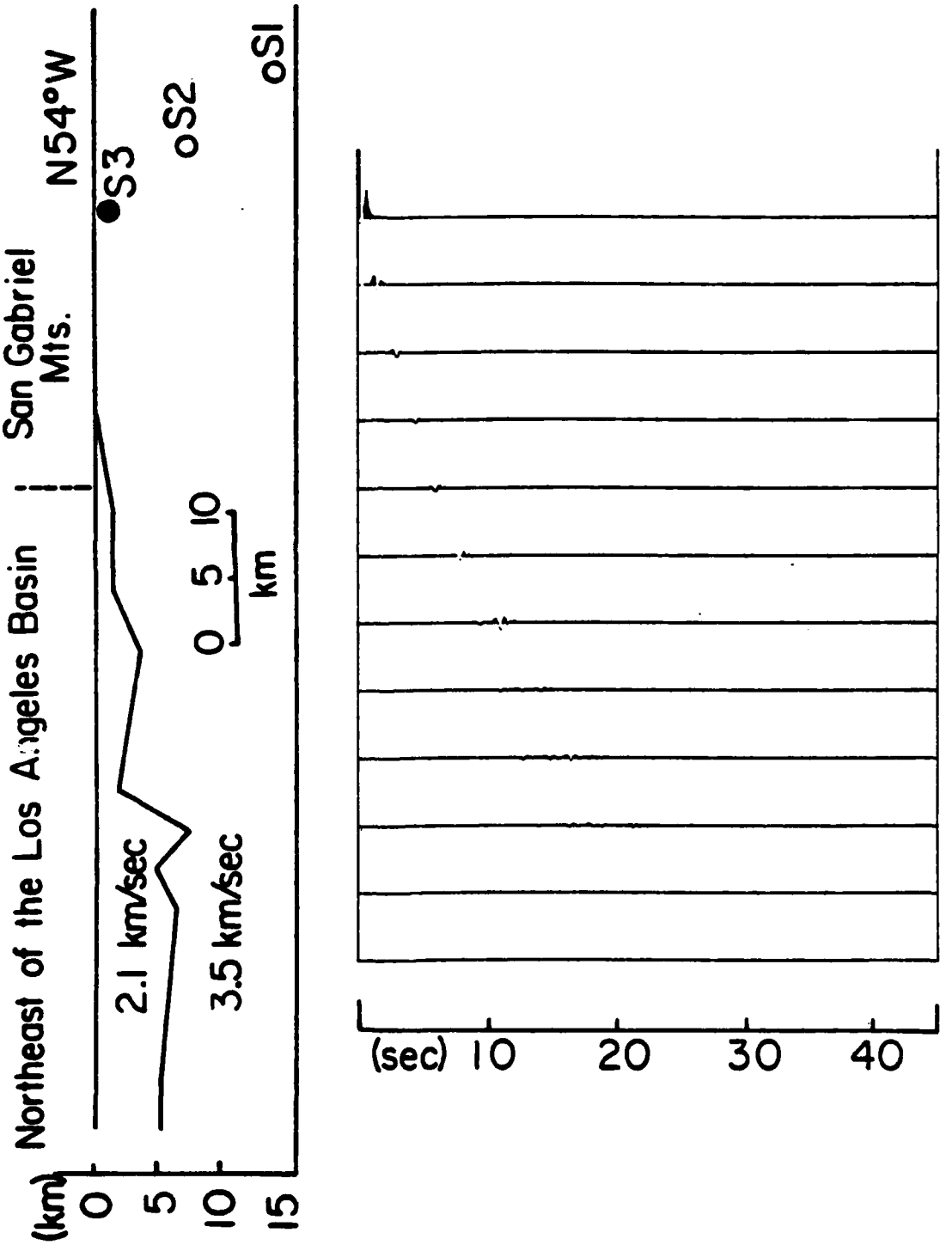


Figure 3-18(c) Synthetic seismograms along profile II from a source at a depth of 1 km.

Los Angeles Basin, the wave development is quite different from that seen along profile I. We approximate the structure along this profile as a basin ( shear velocity of 2.1 km/sec ) embedded in a half-sapce ( 3.5 km/sec ), as illustrated in the left of Figure 3-18(a). In spite of this rather simplified structure model , the synthetics compare well with the motions observed along profile II ( Figure 3-5 ).

As was the case for profile I, that the S! phase is primarily composed of direct S-wave arrivals from S1 ( source at 13 km ). In our synthetics, surface waves are gradually developed after distance of about 40 km, which agrees well with the observations. According to our 2D modeling, the shallow source (S3) contributes little to ground motions observed along this path. Because the structure in the source region is approximated by a half-space, little energy from the shallow source is trapped within the basin.

**Discussions and Conclusions**

Velocity profiles recorded from the 1971 San Fernando earthquake demonstrate strong path effects due to topography of the basement surfaces. The different waveform pattern observed along three long profiles implies that valley or basin structures can produce significant reverberation and amplification effects. It is suggested that the proper geometry of basins and earthquake sources needs to be considered in order to predict waveforms along these wave paths.

Velocity profiles along three local arrays in the Los Angles basin suggests that, within 3 km in range, the waveforms are almost identical. It is also suggested that higher frequency waves, as represented by ground accelerations,

are less affected by these large scale basin structures.

Profiles of displacement traces, which are not shown in this study, display characteristics similar to those observed in the velocity profiles. That is, the waveforms show good correlation with variations in the basement surfaces. However, due to its high-frequency nature, the S! phase is more easily recognized in velocity records than in displacement records.

Along profile III, displacements have relatively simple waveform. This is consistent with our understanding of the basement surface along profile II, since a half-space seems to be an adequate approximation for the propagating path. We speculate that only deeper sources effectively transmit short-period energy along this profile as suggested in Figures 3-18(a) through 3-18(c). This is probably the main reason that the duration of high-frequency motion is rather short for all the stations recorded along this azimuth.

We use the 2D finite difference method to compute synthetic seismograms for irregular structures which exist along profile I and profile II. Although the structure used in the calculation is rather simplified and the numerical code is for acoustical media, the general features of the synthetics agree quite well with the observed ground motions. We approximate Heaton's ( 1982 ) source model, which has two major areas of dislocation by point sources , at depths of 13 km and 1 km. Using the relative timing, amplitude and signal duration of major arrivals observed in the ground motions along both profile I and profile II, we suggest that the coherent S! phase ( the S waves ) is primarily from the first source, at 13 km. The shallow source ( near 1 km ) contributes little to the stations along the profile II. However, it does produce strong surface waves for the stations in the San Fernando Basin region and also contributes to the generation

of surface waves in the Los Angeles Basin. This study suggests that the observed ground motions are indeed affected strongly by propagation paths along different structural provinces.

**References**

Abdel-Ghaffar A. M. and R. F. Scott ( 1978 ), An investigation of the dynamic characteristics of an earth dam, REPORT NO. EERL 78-02, California Institute of Technology

Aki K. ( 1968 ), Seismic displacements near a fault, J. of Geoph. Res., 73, 5359-5376.

Aki K. ( 1979 ), Characterization of barriers on an earthquake fault, J. of Geoph. Res., 84, 6140-6148.

Allen, C. R., T. C. Hanks, J. H. Whitcomb ( 1973 ), San Fernando earthquake: Seismological studies and their implications in San Fernando California Earthquake of February 9, 1971, Vol. I, Geological & Geophysical Studies, U. S. Government Printing Office, Washington, D. C.

Anderson J. G. and T. H. Heaton ( 1979 ), Aftershock accelerograms recorded on a temporary array, U. S. Professional Paper.

Angstman B. G., P. K. P. Spudich and J. Fletcher ( 1979 ), The Coyote Lake earthquake : 0.42 G acceleration from an S-P converted phase, Trans. Am. Geoph. Un., 60, No. 46, S 121.

Archuleta, R. ( 1979 ), Rupture propagation effects in the Coyote Lake earthquake, EOS, 60, No. 46, Nov. 13, S 122.

Archuleta, R. J. and S. M. Day ( 1980 ), Dynamic Rupture in a layered medium: The 1966 Parkfield earthquake, 70, 671-689.

Boore, D. M., W. B. Joyner, A. A. Oliver, III and R. A. Page ( 1980 ), Peak acceleration, velocity and displacement from strong-motion records, Bull. Seis. Soc. Am., 70, 305-321.

Boore, D. M. and M. D. Zoback ( 1974 ), Near-field motions from kinematic models of propagating faults, Bull. Seis. Soc. Am., 64, 321-342.

Bouchon M. and K. Aki ( 1979 ), Predictability of ground displacement and

velocity near an earthquake fault: An example: The Parkfield earthquake of 1966, J. of Geoph. Res., 84, 6149-6156.

Bouchon, M. ( 1982 ), The rupture mechanism of the Coyote Lake earthquake of 6 August 1979 inferred from near-field data, Bull. Seism. Soc. Am., 72, 745-757.

Brady, A. G., P. N. Mork, V. Perez and L. Porter ( 1979 ), Processed data from the Gilroy array and Coyote Creek records, Coyote Lake, California earthquake 6 August 1979, USGS OPEN-FILE REPORT, 81-42.

Brady, A. G., V. Perez and P. N. Mork ( 1980 ), The Imperial Valley earthquake, October 15, 1979, digitization and processing of accelerograph records, USGS OPEN-FILE REPORT, 80-703.

Brady, A. G. and R. L. Porcella ( 1982 ), Imperial Valley aftershocks during the first 24 hours; A discussion of the strong-motion records ( in press ).

Brown, D. and R. Clayton ( 1983 ), Difference approximations for forward modeling problems ( in preparation ).

Burdick, L. J. and C. A. Langston ( 1977 ), Modeling crustal structure through the use of converted phases in teleseismic body-wave forms, Bull. Seism. Soc. Am., 67, 677-691.

Carpenter, E. W. ( 1967 ), Teleseismic signals calculated for underground, underwater, and atmospheric explosion, Geophysics, 32, 17-32.

Duke, C. M. and A. M. Mal ( 1978 ), Site and source effects on earthquake ground motion, NSF GRANT REPORT G144056, UCLA.

Eaton, J. P., M. E. O'neill and J. M. Murdock ( 1970 ), Aftershocks of the 1966 Parkfield Cholame, California earthquake: A detailed study, Bull. Seis. Soc. Am., 60, 1151-1197.

EERL, Caltech ( 1974 ), Strong Motion Earthquake Accelerrgrams, Vol. II, Report from Earthquake Engineering Research Laboratory, California Institute of Technology.

Fuis G. S., W. D. Mooney, J. H. Healy and G.A. McMechan and W. J. Lutter ( 1981 ),

Crustal structure of the Imperial Valley region, USGS OPEN-FILE REPORT.

Hadley, D. M., D. V. Helmberger and J. A. Orcutt ( 1982 ), Peak acceleration scaling studies, Bull. Seis. Soc. Am., 72, 959-979.

Hanks, T. C. ( 1975 ), Strong ground motion of the San Fernando, California earthquake: Ground displacements, Bull. Seism. Soc. Am., Vol. 65, No. 1, 193-225.

Hartzell, S. T. ( 1978 ), Interpretation of earthquake strong ground motion and implications for earthquake mechanism, Ph.D. Dissertation, U. C. San Diego, 115-119.

Hartzell, S. T. ( 1980 ), Faulting process of the May 17, 1976 Gazli, USSR earthquake, Bull. Seism. Soc. Am., 70, 1715-1736.

Hartzell, S. T. and D. V. Helmberger ( 1982 ), Strong-motion modeling of the Imperial Valley earthquake of 1979, Bull. Seis. Soc. Am., 72, 571.

Heaton, T. H. and D. V. Helmberger ( 1978 ), Predictability of strong ground motion in the Imperial Valley: Modeling the $M_L$ 4.9, November 4, 1976 Brawley earthquake, Bull. Seism. Soc. Am., 68, 31-48.

Heaton T. H. and D. V. Helmberger ( 1979 ), Generalized ray models of the San Fernando earthquake, Bull. Seis. soc. Am., 1131-1341.

Heaton, T. H. ( 1982 ), The 1971 San Fernando earthquake: A double event?, Bull. Seis. Soc. Am., 2037-2062.

Helmberger, D. G. and G. Engen ( 1980 ), Modeling the long-period body waves from shallow earthquakes at regional ranges, Bull. Seism. Soc. Am., 70, 5, 1699-1714.

Helmberger, D. V., G. Engen and P. Scott ( 1979 ), A note on velocity density and attenuation models for marine sediments, J. Geoph. Res., 84, 667-671.

Helmberger, D. G. adn D. G. Harkrider ( 1978 ), Modeling earthquakes with generalized ray theory, Proceedings of IUTAM Symposium: Modern Problems In Elastic Wave Propagation, published by John Wiley & Sons, Inc., 499-518.

Herd, D. G., R. J. Mclaughlin, A. M. Sarna-Wojcicki, M. M. Clark, W. H. K. Lee, R. V. Sharp, D. H. Sorg, W. D. Stuart, P. W. Harsh and R. K. Mark ( 1979 ), Surface faulting accompanying the August 6, 1979 Coyote Lake earthquake, EOS, 60, No. 46, 890.

Langston, C. A and D. V. Helmberger ( 1975 ), A procedure for modeling shallow dislocation source, Geophs. J. Res. Astron. Soc., 42, 117-130.

Le Bras, R. ( 1982 ), An inversion algorithm for strong ground motion data application to the 1979 Imperial Valley earthquake ( in preparation ).

Lee, W., D. Herd, V. Cagnetti, W. Bakun and A. Rapport( 1979 ), A preliminary study of the Coyote Lake earthquake of August 6, 1979 and its major aftershocks, USGS OPEN-FILE REPORT 79-1621.

Lindh, A. G. and D. M. Boore ( 1981 ), Control of rupture by fault geometry during the 1966 Parkfield earthquake, Bull. Seism. Soc. Am., 71, 95-116.

Lindh A. G., D. M. Boore, P. Mutch and D. Reneau ( 1982 ), future studies on the 1966 Parkfield earthquake ( in press ).

Johnson, C. E. and L. K. Hutton ( 1981 ), Aftershocks and prior seismicity of the 1979 Imperial Valley earthquake, U. S. Geological Survey open-file report, Menlo Park.

Joyner, W. B., R. E. Warrick and T. E. Fumal ( 1981 ), The effect of Quaternary alluvium on strong-ground motion in the Coyote Lake, California earthquake of 1979, Bull. Seis. Soc. Am., 71, 4, 1333.

Madariaga, R. ( 1977 ), High-frequency radiation from crack ( stress drop ) models of earthquake faulting, Geophys. J. Res. Astro. Soc., 51, 625-651.

Mellman, G. R. and D. V. Helmberger ( 1974 ), High-frequency attenuation by a thin high-velocity layer, Bull. Seism. Soc. Am., 64, 1383-1388.

Mellman, G. R. ( 1978 ), A method for waveform inversion of body-wave seismograms, Ph.D. Thesis, California Institute of Technology, Pasadena.

Nabelek, J. ( 1982 ), Teleseismic constraints on the 1979 Coyote Lake and 1981 El

Asnam earthquake ( in press ).

Olson, A. H. ( 1982 ), The discrete wavenumber/finite element method for synthetic seismograms, Part I, Ph.D. Thesis, U. C. San Diego.

Rial, J. A. and P. Scott ( 1983 ), Ray path effects in strong motion seismology: Caustics and focusing by sedimentary basins ( in preparation ).

Trifunac, M. D. ( 1974 ), A three dimensional dislocation model for the San Fernando, California earthquake of February 9, 1971, Bull. Seis. Soc. Am., 64, 149-172.

Trifunac, M. D. and F. E. Udwadia ( 1974 ), Parkfield, California earthquke of June 27, 1966: A three dimensional moving dislocation, Bull. Seism. Soc. Am., 64 , 511-533.

Trifunac, M. D. ( 1976 ), Preliminary analysis of the peaks of strong ground motion; Dependence of peaks on earthquake magnitude, epicentral distance, and recording site conditions, Bull. Seism. Soc. Am., 66, 189-219.

Uhrhammer, R. ( 1980 ), Observations of the Coyote Lake, California earthquake sequence of August 6, 1979, Bull. Seism. Soc. Am., 70, 559-570.

Wallace, T., D. V. Helmberger and G. Mellman ( 1981 ), A technique for the inversion of regional data in source parameter studies, J. Geophs. Res., 86, 1679-1685.

Yerkes, R. F., T. H. McCulloh, J. E. Schoellhammer and J. G. Vedder ( 1965 ), Geology of the Los Angeles Basin California-- An introduction, Geological Survey Professional Paper 420-A.

END

FILMED

10-84

DTIC